frontiers | Frontiers in Ecology and Evolution

TYPE Original Research
PUBLISHED 17 December 2025
DOI 10.3389/fevo.2025.1669055

OPEN ACCESS

EDITED BY
Gabriel de Souza Ferreira,
Senckenberg Research Centre for Human Evolution and Palaeoenvironment (S-HEP), Germany

REVIEWED BY
Yue Liang,
Northwest University, China
Lara Maldanis,
Université Grenoble Alpes, France

*CORRESPONDENCE
Gabriel Ladeira Oses
gabriel.oses@alumni.usp.br

RECEIVED 18 July 2025
REVISED 03 November 2025
ACCEPTED 12 November 2025
PUBLISHED 17 December 2025

CITATION
Oses GL, Belatto SL, Limeira Junior SCM, dos Santos TP, Rodrigues CL, Prado GMEM, Dias J, Carvalho IDS, da Silva TF and Rizzutto MdA (2025) Imaging and spectroscopy techniques applied to characterise fossilisation processes and biomineralisation.
Front. Ecol. Evol. 13:1669055.
doi: 10.3389/fevo.2025.1669055

Imaging and spectroscopy techniques applied to characterise fossilisation processes and biomineralisation

Gabriel Ladeira Oses[1]*, Sabrina Larissa Belatto[2], Silvio Cesar Marqui Limeira Junior[3], Túlio Paulino dos Santos[1], Cleber Lima Rodrigues[4], Gustavo Marcondes Evangelista Martins Prado[5], Jaime Dias[6], Ismar De Souza Carvalho[6], Tiago Fiorini da Silva[4] and Marcia de Almeida Rizzutto[1]

[1]Laboratório de Arqueometria e Ciências Aplicadas ao Patrimônio Cultural (LACAPC), Instituto de Física, Universidade de São Paulo, São Paulo, SP, Brazil, [2]Programa de Pós-Graduação em Ecologia e Recursos Naturais (PPGERN), Universidade Federal de São Carlos, São Carlos, SP, Brazil, [3]Programa de Pós-Graduação em Física, Instituto de Física, Universidade de São Paulo, São Paulo, SP, Brazil, [4]Laboratório de Análise de Materiais por Feixes Iônicos (LAMFI), Instituto de Física, Universidade de São Paulo, São Paulo, SP, Brazil, [5]Instituto de Química, Universidade de São Paulo, São Paulo, SP, Brazil, [6]Instituto de Geociências, Universidade federal do Rio de Janeiro, Rio de Janeiro, RJ, Brazil

Palaeontology has long benefited from advancements in technology, allowing more refined morphological and compositional characterisation of fossils, relying on non-destructive and non-invasive techniques. Besides the improvement of existing technology and the development of new instruments, techniques, and data processing methods, the combination of imaging and of spectroscopy techniques lay at the core of palaeometry, as it has proven to be a powerful approach to disentangle morphological and geochemical diagenetic imprints, which potentially bias the identification of primary signals in fossils, those of which have palaeobiological significance. This rationale is applicable to the investigation of soft-tissue mineralisation and to the study of the earliest biomineralising animals, in which diagenesis affects primary composition and morphology. Here, we show the application of ionoluminescence (IL) by means of proton beams in an accelerator to yield images of unprepared calcareous fossils (earliest skeletal animals from the Ediacaran Tamengo Formation, Brazil) and of fossils preserved in carbonate rocks (fossil insects from the Cretaceous Crato Formation, Brazil), discussing the benefits of this method over conventional cathodoluminescence (CL). We also provide a UV-light-based imaging (ultraviolet fluorescence photography, UVF) study of the same array of fossils, which enabled the distinction of different mineralogical compositions at

fossil insects. This imaging technique has guided the application of X-ray fluorescence (XRF) and micro-Raman spectroscopy (micro-RS) techniques, confirming heterogeneous mineralogical compositions over the fossils. Finally, radiography of these fossil insects (and arachnids) reveals the potential of this technique to the characterisation of internal soft tissues and of morphological features hidden in the calcareous host rock of the Crato Fm. fossils, thus improving taxonomic identification in a non-destructive way.

KEYWORDS

palaeometry, imaging techniques, spectroscopic techniques, fossilisation, biomineralisation, ionoluminescence, UV photography, radiography

1 Introduction

New scientific challenges always push researchers to improve their methodological approaches for data retrieval of research materials. As a result, previous assessments can be refined, and new protocols for analysing different materials are developed, which may in turn expand the frontiers of knowledge by better assessing the scientific known unknowns. The aim of establishing a non-destructive and ideally non-invasive analysis in the study of rare and valuable samples aids in the preservation of cultural or palaeontological/geological heritage, granting the replication of studies by independent research groups, resulting in hypothesis testing, thus strengthening theories. The combination of imaging and spectroscopy techniques, together with image processing, and the development of new methods and protocols for analysing fossils, are integrated into the field of palaeometry (Riquelme et al., 2009; Delgado et al., 2014) and are increasingly demanded in paleontological studies. We present a brief historical overview of the application of selected imaging methods in palaeontology.

Among imaging techniques, luminescence of minerals stimulated by an excitation source (either particles or radiation) has a wide application to numerous branches of Science (Yang et al., 1994; Stoneman et al., 2024). In geosciences, the analysis of luminescence is commonly used to carbonate petrology, in which it is paramount to refine the habits and arrangement of mineral phases, enabling cement stratigraphy, which helps in constraining carbonate diagenesis of fossils and rocks (Machel, 2000). Luminescence imaging also enhances the morphology of calcareous fossils, thus providing images for new morphological reconstructions. For instance, using cathodoluminescence (CL), the skeletal construction of the Ediacaran biomineralising metazoan *Corumbella werneri* was reinterpreted, thus creating basis for the revaluation of its biological affinity (Osés et al., 2022). Luminescence also helps in indirectly tracking the diagenetic incorporation of metals in carbonates (e.g., Machel, 2000; Osés et al., 2022). The cathodoluminescence technique is commonly used in other areas of geosciences (Machel, 2000).

Ionoluminescence (IL) coupled to PIXE (particle-induced X-ray emission) in geosciences are used to explain carbonate luminescence and REE (rare-earth element) incorporation in different minerals; to track zircon alteration zonation aiming to select the most preserved crystal regions for geochronology; to determine the oxidation state of a given element in a mineral (Yang et al., 1994); and, to investigate ion beam damage by PIXE (Enguita et al., 2004).

Visible fluorescence induced by ultraviolet (UV) light is a useful imaging technique in palaeontology (ultraviolet fluorescence photography, UVF), as it optimises information retrieval from fossils, like enhancing fossil morphology in a host rock of different composition (Riquelme et al., 2009; Haug et al., 2009; Tischlinger and Arratia, 2013; Crippa and Masini, 2022; Boderau et al., 2024). This method also allows the recognition of preserved soft tissues (Wang et al., 2017; Liu et al., 2019; Klug et al., 2019; Crippa and Masini, 2022), of original colour-patterns in fossils (Kelley and Swann, 1988; Wolkenstein, 2022; Wolkenstein et al., 2024), and enables the reconstruction of palaeobiological and palaeoecological interactions (Klug et al., 2016, 2021a, 2021b; Boderau et al., 2024). Additionally, this technique is used to recognise preservational modes aided by geochemical techniques (Frese et al., 2017; Crippa and Masini, 2022; Delsett et al., 2022; Boderau et al., 2024). In taphonomy, UVF can be used as a tool to guide subsequent geochemical analyses (Riquelme et al., 2009).

Raman spectroscopy (RS) and X-ray fluorescence (XRF) are complementary techniques widely used in the non-destructive compositional characterisation of fossils. These are particularly useful for analysing fossilised soft tissues, diagenetic minerals, and signals of preserved organic matter (specially by RS characterisation). For instance, Choi et al. (2020) used RS to detect amorphous carbon in fossil eggs possibly attributed to non-dinosaurian archosaurs, recovered from the Upper Cretaceous volcanic deposits of Wido, South Korea. XRF, in turn, allows for determination of elemental composition and is widely applied to assess the incorporation of elements during fossilisation (Osés et al., 2016, 2017). In the Crato Formation, these techniques have played a central role in the development and refinement of taphonomic models. Osés et al. (2016, 2017) used RS and XRF to propose a model based on the compartmentalisation of pyritisation

and kerogenisation processes across different lithofacies. Subsequently, Bezerra et al. (2018) applied RS to document kerogenisation in fossil insects - previously reported only in fossilised fishes (Osés et al., 2017) - and demonstrated the coexistence of distinct preservation modes in the same lithofacies. Bezerra et al. (2020) identified signals of preserved organic matter in pyritised insects from beige limestones, suggesting a broader diversity of taphonomic pathways for this lithofacies. These developments underscore the key role of such techniques in advancing the understanding of the geochemical processes governing fossilisation in exceptional preservation contexts.

Radiography and tomography are X-ray imaging techniques applied to study the interior of objects (Lang and Middleton, 2005). X-ray based imaging techniques consist in a widely applied, non-destructive, approach in fossil studies, as they allow the non-invasive preparation of specimens. For instance, researchers used tomography to identify marks made by insects in vertebrate bones from the Triassic of Brazil (Paes-Neto et al., 2016). Using synchrotron X-ray tomography (Prado et al., 2021), researchers were able to identify the fossilised heart of exceptionally preserved fish from the Cretaceous of Brazil (Maldanis et al., 2016), whilst others could reconstruct the 3D anatomy of a well-preserved beetle fossil from the Oligocene of Quercy phosphorite Formation of France (Schwermann et al., 2016). Heads and Martins-Neto (2007) analysed a Crato Formation orthopteran with tomography showing likely soft-tissue preservation, and Carvalho et al. (2023) used micro-CT to visualise anatomical details of a scorpion from the Crato Fm.

Fossils of the Ediacaran metazoan *Corumbella werneri* from the Tamengo Formation (Brazil) were analysed using IL and UVF, respectively aiming to validate the former technique for the characterisation of carbonate skeletal fossils and to test whether the latter could yield yet undetermined morphological or compositional information. Fossil insects from the Crato Formation (Brazil) were analysed with IL, UVF and radiography, the latter also used to image an arachnid from this geological unit. These techniques were used respectively aiming (1) to test the IL imaging of totally unprepared large carbonate samples bearing fossils, (2) to use UV to probe differences in fossil compositions, and (3) to yield images of internal structures and features hidden within the host rock. UVF guided subsequent complementary XRF and micro-RS analyses, which explained the fluorescence heterogeneities of samples. IL image mapping and processing of fossils was developed in the Institute of Physics/University of São Paulo by the LACAPC (Laboratory of Archaeometry and Sciences Applied to the Cultural Heritage) and LAMFI (Laboratory of Materials Analyses by ionic beams) teams. Radiography parameters (voltage, current and time) testing was performed aimed to create a guideline for researchers working with samples of similar composition and interested in refining taxonomic identification by observing diagnostic features covered by the host rock, and in imaging soft-tissue preservation, respectively without removing host rock nor destroying the sample.

2 Overview of the applied techniques

2.1 Luminescence-based imaging techniques

In general terms, luminescence is the emission of light from a sample excited electronically or vibrationally without heating (Gaft et al., 2015; IUPAC, 2025). This phenomenon can be subdivided based on the source of stimulation, such as photoluminescence (low-energy photons), bioluminescence (biochemical reaction), cathodoluminescence (high-energy electrons), radioluminescence (ionising radiation), ionoluminescence (ion beam), piezoluminescence (induced pressure), among others (Nair and Dhoble, 2020). Photoluminescence is divided into two distinct phenomena, fluorescence and phosphorescence, which basically depends on the material being irradiated and differs in the way the radiation interacts with the object and how light is emitted (Nair and Dhoble, 2020). In the former type, light is only emitted during excitation, while in the latter, as object absorbs radiation, light emission continues even after excitation ceases. Because luminescence is characteristic of the material excitation, such as the presence of elemental species or their chemical bonds, many properties can be studied, especially through imaging.

Luminescence induced by ion beams (IL) is a type of fluorescence characterised by visible light emission by a target irradiated with an ion beam with energy in the range of MeV/amu (megaelectron volt/atomic mass unit) (Yang et al., 1994). The resulting emitted photons are due to the energy transferred from the ion beam to the electrons of the targeted material by absorbance, which increases electron excitation from the ground to the excited state. More specifically, ion beam-material interaction yields secondary emission of photons, whose energy is absorbed by the material, leaving it ionized, and energy is transmitted to the crystal lattice, followed by de-excitation of highly-excited states, and subsequent further de-excitation to ground level energy, which yields light emission (Yang et al., 1994). The IL phenomenon occurs by the interaction of an ion beam with the outer electrons of atoms, which enables to probe information on the valence, structural defects, chemical bonding, and trace elements of minerals, by analysing the intensity and wavelength of the luminescence spectrum (Yang et al., 1994). This emitted luminescence can be photographed and measured by a spectrophotometer, which can be used to identify emission bands diagnostic of elements associated with minerals.

When a material is excited by light in the UV region of the electromagnetic spectrum (wavelength range of 100–400 nm), the electrons of the material are excited, and when reaching the ground state (stability) photons are emitted as visible light (fluorescence). This process is similar to the fluorescence generated by the interaction of an ion beam with a sample described above, though the energy involved, and thus penetration, are much lower. The visible fluorescence can be captured by photography (UVF).

2.2 X-ray-based imaging (radiography)

X-rays are electromagnetic radiation, with high frequency and low wavelength – 0.01 nm to 10 nm – compared to other radiation in the electromagnetic spectrum, thus causing high energy transfer. When X-ray pass through a sample, it is absorbed proportionally to the material density, thus resulting in a radiographic image of the sample interior (Curry et al., 1990; Langland et al., 2002; Bushberg et al., 2011; White and Pharoah, 2013). Besides absorption contrast, phase contrast is paramount for materials imaging, particularly those with low attenuation (or low absorption, thus being composed by light elements) (Endrizzi, 2018). Overall, phase-contrast imaging relies on the interference of materials in the phase of electromagnetic waves impinging on them (Endrizzi, 2018).

There are some factors that influence the quality of images obtained by radiography (contrast, signal-to-noise-ratio, spatial resolution, and sharpness), including voltage, electrical current, integration time (Lang and Middleton, 2005), the relative distances between the X-ray source and the object and between the object and the detector (Tompe and Sargar, 2022), and detector characteristics (Williams et al., 2007).

2.3 Spectroscopic techniques

The X-Ray Fluorescence (XRF) technique is a non-destructive analytical tool widely used to determine the elemental composition of geological, archaeological and palaeontological materials. Its physical principle is based on the interaction between high-energy photons — generated by an X-ray emitting tube — and the atoms present in the sample, a process that induces the photoelectric effect (Van Grieken and Markowicz, 2001; Jenkins, 1999). When a photon hits an atom, an electron can be ejected from one of its inner shells, creating an electronic vacancy. This vacancy is then filled by an electron from a more outer shell, and the excess energy is released in the form of secondary X-rays (characteristic X-rays). Since each chemical element has a unique set of electronic energy levels, the emitted radiation exhibits characteristic energies specific to that element, which are detected and analysed by a spectrometer, allowing the qualitative identification and, in many cases, a quantitative estimate of the elements present in the sample (Van Grieken and Markowicz, 2001; Jenkins, 1999). In geosciences, XRF is more commonly used for bulk geochemical analysis, but it can also be applied *in situ* and in scanning mode for the generation of elemental maps (Prado et al., 2021).

RS spectroscopy is a non-destructive analytical technique based on the inelastic scattering of monochromatic light, used to investigate the molecular (organic and inorganic) composition of samples. When a sample is targeted by the laser beam, most photons are scattered elastically (Rayleigh scattering); however, a small fraction interacts with the molecules, resulting in an energy shift — the so-called Raman effect (Lewis and Edwards, 2001; Vandenabeele, 2013). This phenomenon occurs when the incident photon excites the molecule to a virtual energy state, from which it returns to a different vibrational level, emitting a photon with altered energy. The energy shifts recorded in the Raman spectrum, expressed in wavenumbers (cm^{-1}), correspond to the specific vibrational modes of the chemical bonds present in the sample. Two types of inelastic scattering can occur: (1) Stokes, when the molecule absorbs energy and the emitted photon has lower energy than the incident one; and (2) anti-Stokes, when the molecule is already in an excited state and transfers energy to the photon, which is then emitted with higher energy. Since most molecules are in the ground state under ambient conditions, Stokes signals are more intense and commonly used for spectral interpretation (Courtois, 1993).

3 Geological and palaeobiological context

3.1 Tamengo Formation

The Tamengo Formation is a lithostratigraphic unit from the Corumbá Group (South Paraguay Belt, Amazon Craton), that outcrops in the Mato Grosso do Sul state, Brazil, ranging from ca. 555 to ca. 542 Ma (Ediacaran-Cambrian transition; Parry et al., 2017). It comprises a mixed siliciclastic-carbonate succession deposited in a carbonate ramp under storm influence (Oliveira et al., 2019; Amorim et al., 2020). The Ediacaran-Cambrian transition witnessed major palaeobiological and biogeochemical changes, including the appearing and diversification of biomineralising metazoans (Wood, 2018), of meiofaunal bilaterians (Parry et al., 2017) and the restructuring of marine redox conditions (Bowyer et al., 2017).

The typical Nama Assemblage biota of the Tamengo Fm. consists of biomineralising skeletal tubular fossils, particularly *Cloudina* (Zaine and Fairchild, 1985) and *Corumbella* (Hahn et al., 1982; Pacheco et al., 2015). The palaeobiota also includes algae (Diniz et al., 2021), conulariids (Van Iten et al., 2016) and ichnofossils (Parry et al., 2017). Recently, Osés et al. (2022) applied imaging and spectroscopic techniques to investigate the morphology and biomineralisation of *Corumbella*. A multi-technique approach also shed light on the palaeoenvironmental conditions of *Corumbella* depositional setting in the Tamengo Formation, proposing a shallower setting than previously considered (Osés et al., 2025), which had been independently suggested by geochemistry (Antunes et al., 2023). Osés et al. (2025) argued that fine siliciclastic facies with sedimentary structures formed by calcareous bioclasts represent an early change of the sedimentary dynamics of shallow siliciclastic facies.

3.2 Crato Formation

The Crato Formation (late Aptian) is a lithostratigraphic unit globally recognised for bearing one of the most important Konservat-Lagerstätten deposits of the Cretaceous (Selden and Nudds, 2012). This unit is part of the Early Cretaceous of the Araripe Basin, a pull-apart sedimentary basin located in

northeastern Brazil, covering the Ceará, Pernambuco, Paraíba, and Piauí states, with predominantly Mesozoic sedimentation (Assine et al., 2014; Arai and Assine, 2020; Vallejo et al., 2023; Carvalho et al., 2024a, 2024b). The Lagerstätte succession of the Crato Formation encompasses a palaeoenvironment interpreted as a large wetland system, influenced by climatic oscillations between more arid and humid periods (Ribeiro et al., 2021). The stratigraphic horizons with accumulations of *Dastilbe* and Ephemeroptera larvae fossils, associated with halite pseudomorphs, indicate occasional episodes of hypersaline waters, linked to the more arid phases (Storari et al., 2021). A rich and diverse biota is preserved within the beige and grey laminated limestones, including fossils of fungi, bacteria, plants, and animals, the latter being mainly represented by fishes and arthropods (Dias et al., 2022).

Among the metazoans, insects represent the most numerous and diverse group within the Crato Formation, with records of 16 orders (Moura-Júnior et al., 2018). This high diversity, along with the abundance of specimens and their relatively small size, facilitates taphonomic studies. In this context, insect fossils from the Crato Formation represent an important source for palaeometric studies, resulting in morphological, taxonomic, palaeoenvironmental, palaeoclimatic, geomicrobiological, and geochemical interpretations. Over the past ten years, taphonomic studies on the Crato Formation fossils have focused especially on insects, with exceptions involving fishes (Osés et al., 2017) and crustaceans (Varejão et al., 2019).

Barling et al. (2015) and Osés et al. (2016, 2017) examined pyritisation, kerogenisation, and phosphatisation authigenesis of insects, introducing the central role of sulphate-reducing bacterial biofilms in fossil preservation at the Crato Fm. Subsequent studies addressed a range of objectives, including detailed morphological and/or taphonomic descriptions focusing on specific arthropod taxonomic groups (Bezerra et al., 2018 – Blattodea; Varejão et al., 2019 – Decapoda; Bezerra et al., 2020 – Ensifera; Dias and Carvalho, 2020 – Grylloidea; Prado et al., 2021 – Coleoptera; Barling et al., 2021 – Odonata; Carvalho et al., 2023 – Scorpiones; Dias et al., 2023 – Ephemeroptera; Storari et al., 2024a – Ephemeroptera and Grylloidea; Buscalioni et al., 2025 – Ephemeroptera); the use of geochemical analyses for palaeoenvironmental inferences (Barling et al., 2020); statistical methods (Bezerra et al., 2021); the role of microbial mats in the fossilisation process (Iniesto et al., 2021; Dias and Carvalho, 2022; Dias et al., 2023); effects of weathering on fossil preservation (Bezerra et al., 2023); and, the analysis of soft-tissue preservation identified within fossilised Grylloidea carcasses (Osés et al., 2016; Storari et al., 2024b; Dias et al., 2025). Most of these studies were conducted using a wide range of palaeometric tools, such as scanning electron microscopy (SEM), energy dispersive X-ray spectroscopy (EDX), energy dispersive X-ray fluorescence (EDXRF), synchrotron micro-XRF and soft X-ray spectroscopy (SXS), PIXE, micro-RS, petrographic microscopy, and computed microtomography.

4 Materials and methods

4.1 Materials

The analysed *Corumbella* fossils (3 samples; CPL/1-044, CPL/1-045A, and CPL/1-045B) and rock sample bearing bioclasts were collected in the Sobramil Mine outcrop, from the Tamengo Formation, Corumbá Group, located in the city of Corumbá, Mato Grosso do Sul, Brazil. The fossil samples are deposited in the palaeontological collection from the Laboratory of Archaeometry and Sciences Applied to the Cultural Heritage (LACAPC), Institute of Physics, University of São Paulo (USP), Brazil. The fossil arthropods from the Crato Formation (7 samples; GP/1E 7268, GP/1E 10609, GP/1E 11237C, GP/1E 10751, GP/1E 10829, GP/1E 9882, and PF 91/3485/97) belong to the Palaeontological Collection from the Institute of Geosciences, University of São Paulo, Brazil.

4.2 Methods

4.2.1 IL photography

Photography of the IL analysis of samples were taken at the LAMFI, Institute of Physics, University of São Paulo (Figure 1; Supplementary Figure 1). Samples were attached to an automated sample holder, in front of the external proton beam setup from the accelerator. The proton beam targeted the sample with an energy of 2.6 MeV in an area of ca. 30 mm^2, resulting in fluorescence. Image capture was done by a Canon SL3 camera with Canon EF 50 mm f/1.8 STM and Canon EF-S 18–135 mm f/3.5-5.6 STM lenses and, for higher magnification, with the additional use of a 21 mm extension tube (enabling magnification between 0.21x and 0.63x). The choice of lenses was based on required field of view, magnification, and depth of focus. Photographs were made focusing on each point targeted by the proton beam, by moving the sample with the automated sample holder, in order to cover the entire desired area, thus yielding a database for creating an IL map of the samples. Later, photographs were merged and edited in the software Adobe Photoshop and Adobe Lightroom.

Light spectral measurements were performed in luminescent spots representative of carbonate rocks and fossils, by using an optical fibre attached to an OceanOptics USB 4000 spectrophotometer connected to a notebook with a controlling software (Figure 1; Supplementary Figure 1). The measurements were made with a beam energy of 2.6 MeV in an area of 1 mm^2, during 30 s and with 3 averaged spectra.

4.2.2 Photography of visible fluorescence induced by ultraviolet light

The photographs were taken at the LACAPC, Institute of Physics, University of São Paulo (Figure 1; Supplementary

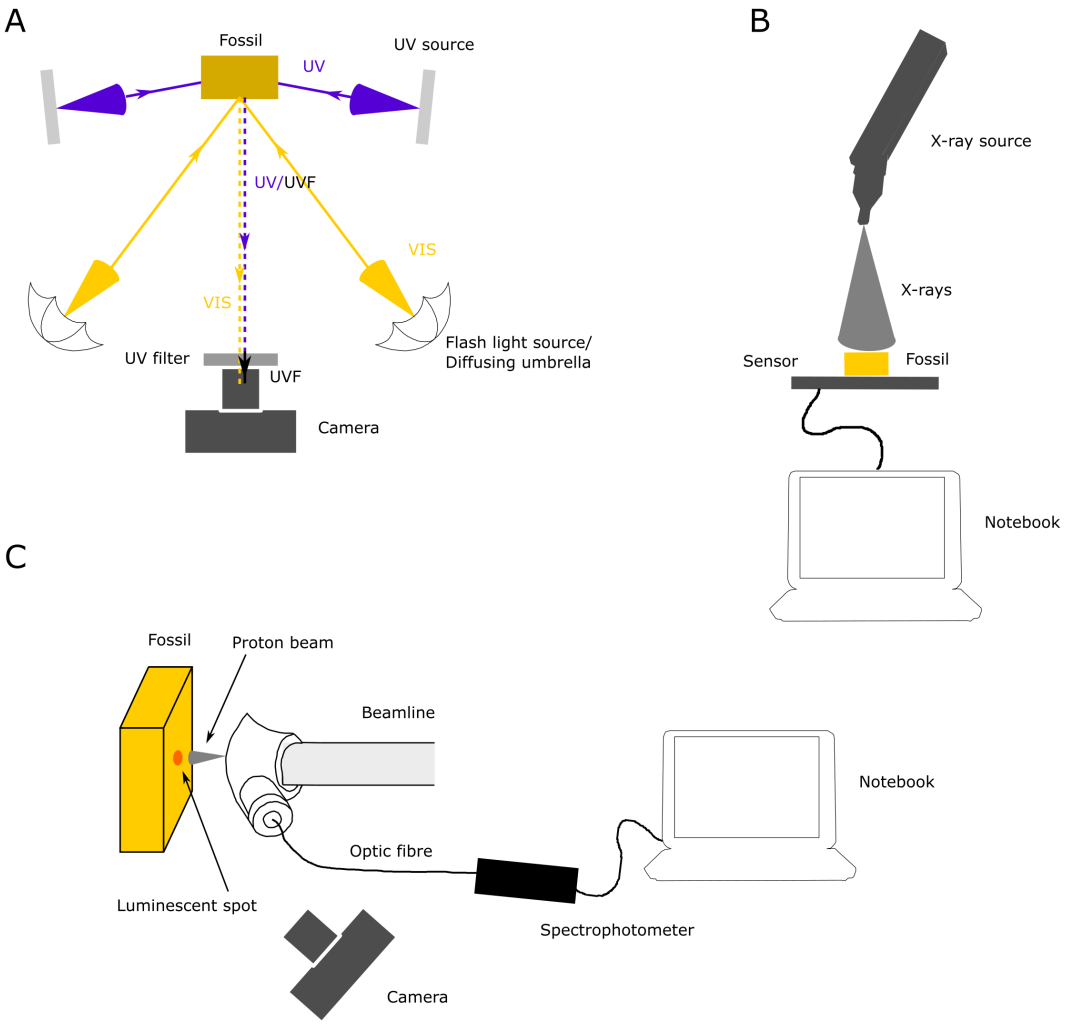

FIGURE 1
Schematic diagrams of the applied techniques. **(A)** Ultraviolet fluorescence photography-visible light photography (UVF-VIS). **(B)** Digital radiography. **(C)** Ionoluminescence (IL).

Figure 2). A Canon EOS R camera coupled with a Canon RF 24-105mm f/4L IS USM lens, and a Nikon D90 camera with a AF-S Micro NIKKOR 105 mm 1:2.8 G ED lens, were used. Both Hoya and Kenko UV filters were, respectively mounted on the lenses. This is important to block either direct UV light produced by the sources, reflected from the sample, or produced by lens fluorescence, allowing only visible light resulting from the fluorescence of UV-object interaction to be captured by the camera sensor (Crowther, 2022). A black blanket was placed beneath the samples to avoid reflectance (Crowther, 2022). Camera alignment was set using a bubble level and the internal camera alignment system for the Canon equipment. Two systems of diffusing umbrella and flashlights (DigiFlash® Start 9800) were positioned at the same distance from the object and symmetrically to each other, both at an angle of 45°from the centre of the object. A radio flash system was used to synchronise photographs with flashlight emission, while using continuous lighting. The lens autofocus option was set for visible light (VIS) and UVF. Continuous lighting was used as to yield enough light to set autofocus with a remote camera shutter connected to the camera whenever it was necessary, avoiding destabilisation of the system. The UV fluorescence resulting from object-UV light interaction was produced by two independent UVA light setups, each with four 125 W and 365 nm light sources. Both setups were positioned close to the samples and at either side of it, and UV-sample interaction fluorescence was visible after a few seconds. Whenever necessary, continuous lighting was used to improve focus detection. Later, photographs were processed in the Adobe Lightroom software.

4.2.3 XRF and micro-RS

Geochemical analyses were carried out using a portable EDXRF system available at the LACAPC. This system consists of a MiniX Amptek silver anode X-ray tube and an Amptek FAST SDD XR-100SDD X-ray detector with a resolution of 125 eV FWHM at the Mn Kα line (5.9 keV) (Supplementary Figure 3). Measurements were performed at 30 kV, 5 μA, with an acquisition time of 100 s per point. Spectral visualisation, calibration, elemental identification, and fitting were conducted using the WinQxas software.

Mineralogical analyses were performed using RS at the Astrolab, Institute of Chemistry, University of São Paulo. The equipment used was a Renishaw inVia Raman system (Supplementary Figure 3) and a 785 nm laser. The acquisition was configured with a static scan centred at 800 cm^{-1}. A microscope with lenses ranging from 50x to 100x were employed to provide different levels of magnification for detailed sample observation. Exposure times varied between 5 s and 30 s. Laser power was set between 0.1% and 1.0% to minimise sample damage while maximising signal detection. The number of accumulations per measurement ranged from 1 to 5 to optimize the signal-to-noise ratio. XRF and micro-RS data treatment was done in the software Spectragryph (Menges, 2022) and Inkscape.

4.2.4 Radiography

Samples used for radiography were photographed with an overhead-mounted Nikon D3200 camera with side illumination, or with an Olympus DSX110 stereomicroscope, respectively at the Palaeontological Collection and the Laboratory of Palaeobiological Studies, Institute of Geosciences, University of São Paulo. These photographs were made aiming to compare the actual samples and the resulting X-ray internal images.

The measurements were performed at the LACAPC. The experimental setup is composed by a MiniX Amptek silver anode X-ray tube and a Carestream Industrex HPX-DR digital detector sensitive to radiation (Figure 1; Supplementary Figure 2).

The distance between the tube and the detector was set to 41 cm. A sequence of measurements was carried out, with different voltage, current and exposure times values (Table 1) for each sample thickness class, until reaching the best possible combination to obtain clear images for samples with different thicknesses. Regarding voltage and current, tests were initially carried out with 40 kV and 99 µA, respectively, but later measurements were carried out with 50 kV and 79 µA. In both cases, an integration time of 10 s and 2 frames were used. Later, the integration time was increased to 100 s with 2 frames resulting in 200 s of exposure time.

Radiographs were also taken using a MAMMOMAT 3000 Nova Siemens equipment, at the Imaging Sector from the University of São Paulo Hospital (HU-USP). The images were acquired with voltage of 29 and 35 kV and with current x time values of 180–320 mA•s (Table 1). These radiographs were digitalised using a conventional scanner, a Canon Powershot SX 110 IS digital camera, and details were photographed in a Zeiss stereomicroscope coupled to a digital camera controlled by the software Zeiss AxioVision, at the Laboratory of Palaeobiological Studies, Institute of Geosciences, University of São Paulo.

After the measurements, the images were edited using the following software: Microsoft PowerPoint/Adobe Photoshop/ImageJ (brightness, sharpness, and contrast) and Inkscape (cropping and repositioning of the scales).

The ImageJ software was also used to improve the quality of the images through the following parameters: Type (16 bits), Enhance Contrast (0.35%), Radius (1.0 to 2.0) and Mask Weight (0.1 to 0.6). 'Type' is the number of binary digits expressed in the image, which allows the recording of more tones of grey. The 'enhance contrast' option increases the contrast of the image. 'Radius' increases image sharpness. 'Mask weight' increases the sharpness of the image, working together with 'Radius'; though high 'Mask weight' values can saturate the image. It was necessary to reduce the brightness of some images since the fossils are brighter than the host rock, as they are denser (iron oxy-/hydroxides and pyrite) relative to the rock (calcite).

A workflow diagram with the ideal sequence for the application of the techniques above is shown in Figure 2. VIS photography precedes UVF since this procedure facilitates the initial visual comparison of resulting fluorescence with the former. Then, to interpret the resulting images, compositional characterisation of the samples is needed, which is done using XRF (for elemental analysis) and subsequently RS (for molecular analysis). These techniques above will enable a better understanding of compositional heterogeneity in samples, supporting more complex IL imaging. VIS photography can be used as a basis of comparison with IL imaging and with radiographies, whose interpretation relies on the elemental compositional (density) of the samples, which can be informed by XRF.

TABLE 1 Parameters used in the radiography analyses.

Parameters	Samples											
	CARESTREAM digital system and Amptek X-ray tube									MAMMOMAT 3000 Nova		
	GP/1E 10609		GP/1E 10829		GP/1E 10751		GP/1E 11237			PF 91/3485/97	GP/1E 9882	
Voltage (kV)	50		50		50		50	40	29	35	35	
Current (µA)/Current x Time (mA•s)	79 µA		79 µA		79 µA		79 µA	99 µA	220 mA•s	180 mA•s	280 mA•s	
Integration time (s)	50	70	50	70	50	70	50	70	10			
Frames	2		2		2		2					
Sample thickness (cm)	1.1		1.2		0.9		1.0			0.7	0.9	
Distance tube-sample (cm)	41		41		41		41		64	64.3	64.1	

10.3389/fevo.2025.1669055

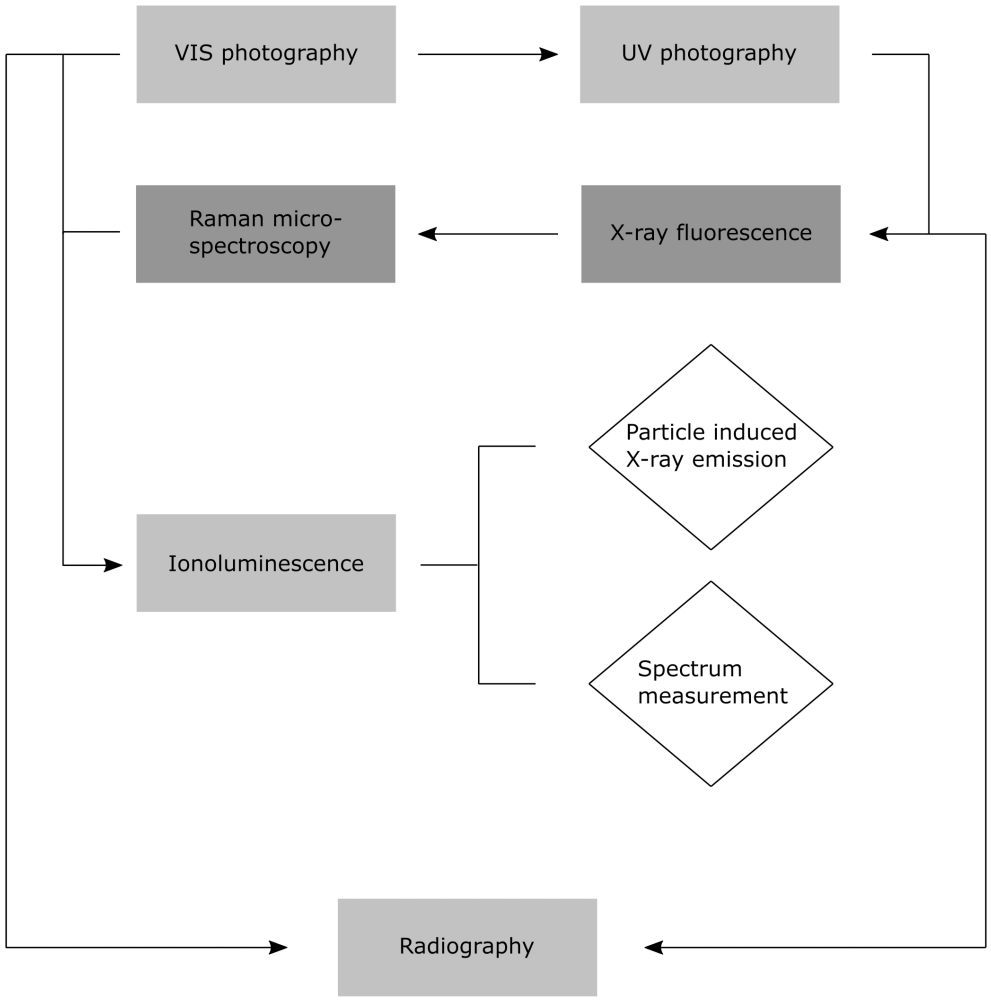

FIGURE 2
Workflow of the application of techniques in this study and possible ideal sequence for other studies.

5 Results

The IL imaging of fossil insects GP/1E 7268 (beige limestone), GP/1E 10609 and GP/1E 11237C (both from grey limestone) show luminescence of the host rock embedding the fossils, and of the rock filling the interior of the fossils, which is exposed where the fossils are cracked (Figure 3). The fossils are non-luminescent. On the other hand, *Corumbella* fossils and carbonate cement in the host rock are luminescent (Figures 4A, B). IL images of a longitudinal section through a *Corumbella*'s tube (Figure 4C) and of a cross-section through the same tube (Figure 4E) show bright luminescent margins of the skeletal elements (plates), while their core is non-luminescent (Figures 4D, F). IL imaging of samples bearing *Corumbella* bioclasts shows different components, such as non-luminescent bioclasts, dull luminescent carbonate, and non-luminescent clay minerals, which altogether form sedimentary structures like bioclastic lenses, pods, and cross-lamination (Figures 4G, H).

The luminescence spectral characterisation in regions taking host rock/fossil of samples GP/1E 7268 and GP/1E 10609 yielded a strong peak in ca. 622 nm (Figures 5A, C). IL of *Corumbella* fossils showed a strong peak in ca. 615 nm and another one in ca. 631 nm (for one measurement only) (Figures 5B, D). These peaks can be attributed to the Mn^{2+} luminescence (Pedone et al., 1990; El Ali et al., 1993 and references therein; Yang et al., 1994; Kusano et al., 2014 and references therein; Romppanen et al., 2021 and references therein).

The interaction of UV light with fossil insects yields dark brown visible fluorescence of originally dark regions (Figures 6A–F), while there is a characteristic emission of bright purple/bluish fluorescence in regions with a white/beige mineral phase in the interior of the fossils (Figures 6C–F; insets of E and F). While irradiated with UV light, the Corumbella fossil does not fluoresce (Figures 6G, H).

Micro-RS analysis shows that the fossil (GP/1E 7268) from beige limestones (BL) is preserved by goethite (Figure 7; bands at 240, 296, 393 and 549/550 cm^{-1}). The beige areas of the fossil (GP/1E 11237C) from grey limestones (GL) have jarosite and characteristic bands related to other sulphate group minerals (Figure 8; bands at 220, 305, 345, 425, 452, 570 ()?, ca. 624, ca. 985, 1005/1006 and 1089/1092 cm^{-1}). The black areas of this fossil

10.3389/fevo.2025.1669055

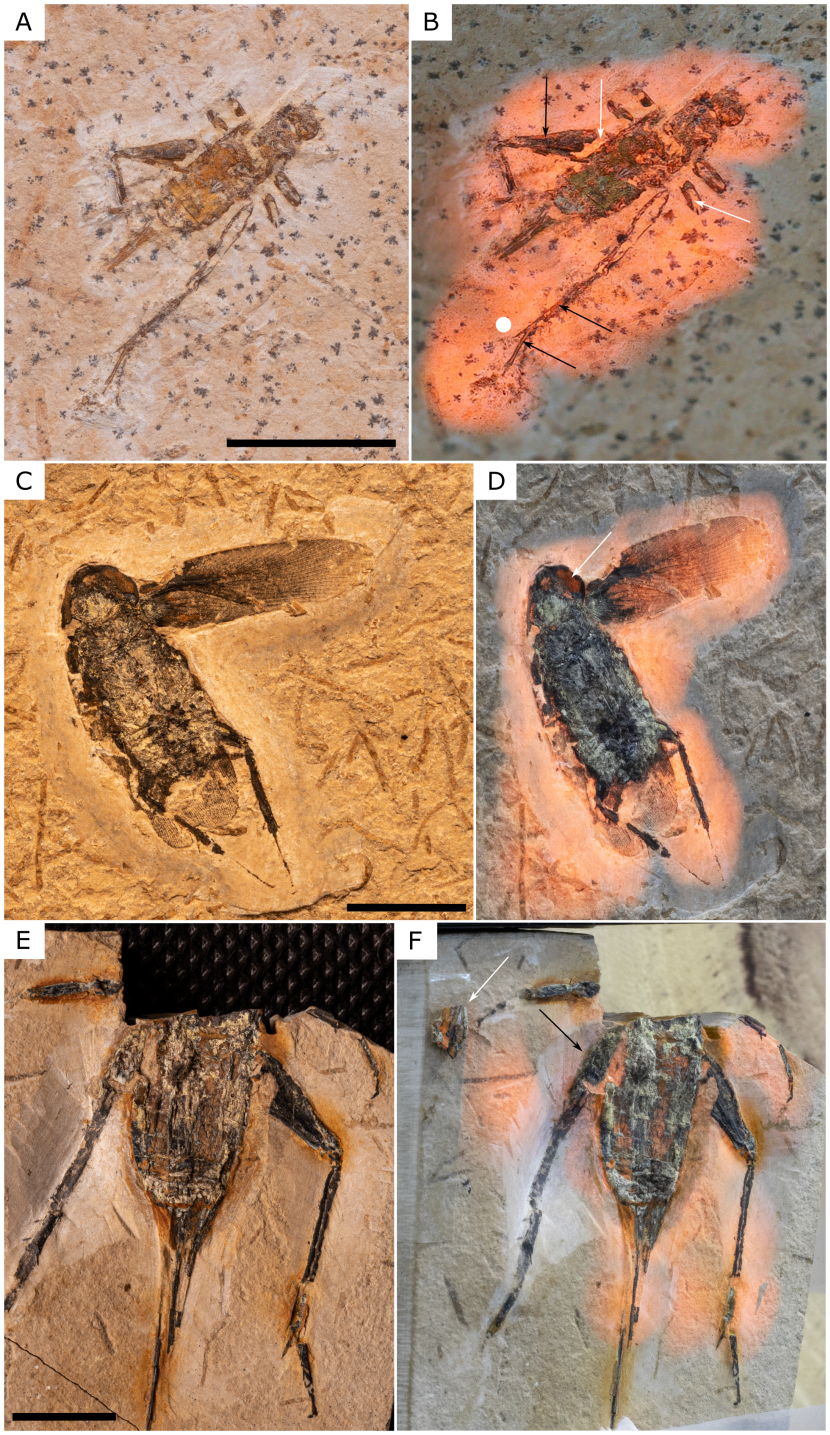

FIGURE 3
Visible light photography of fossils **(A, C, E)** and proton beam-induced luminescence mapping **(B, D, F)**. **(A, B)** Sample GP/1E 7268 (orthopteran from the beige limestone-BL, cf. Osés et al., 2017). Calcite occurs inside the fossil (white arrows). The darker luminescence of some regions of the fossil is indicated by black arrows. The white dot in **(B)** represents the measured spectrum in Figure 5C. **(C, D)** Sample GP/1E 10609 (blattodean from the grey limestone-GL, cf. Osés et al., 2017). The darker luminescence of the internal region of the head is indicated by the white arrow. **(E, F)** Sample GP/1E 11237C (orthopteran from the grey limestone-GL, cf. Osés et al., 2017). The fossil fragment (white arrow) came apart from the right femur of the main specimen (black arrow). Scale bars: **(A, C, E)** – 1 cm.

10.3389/fevo.2025.1669055

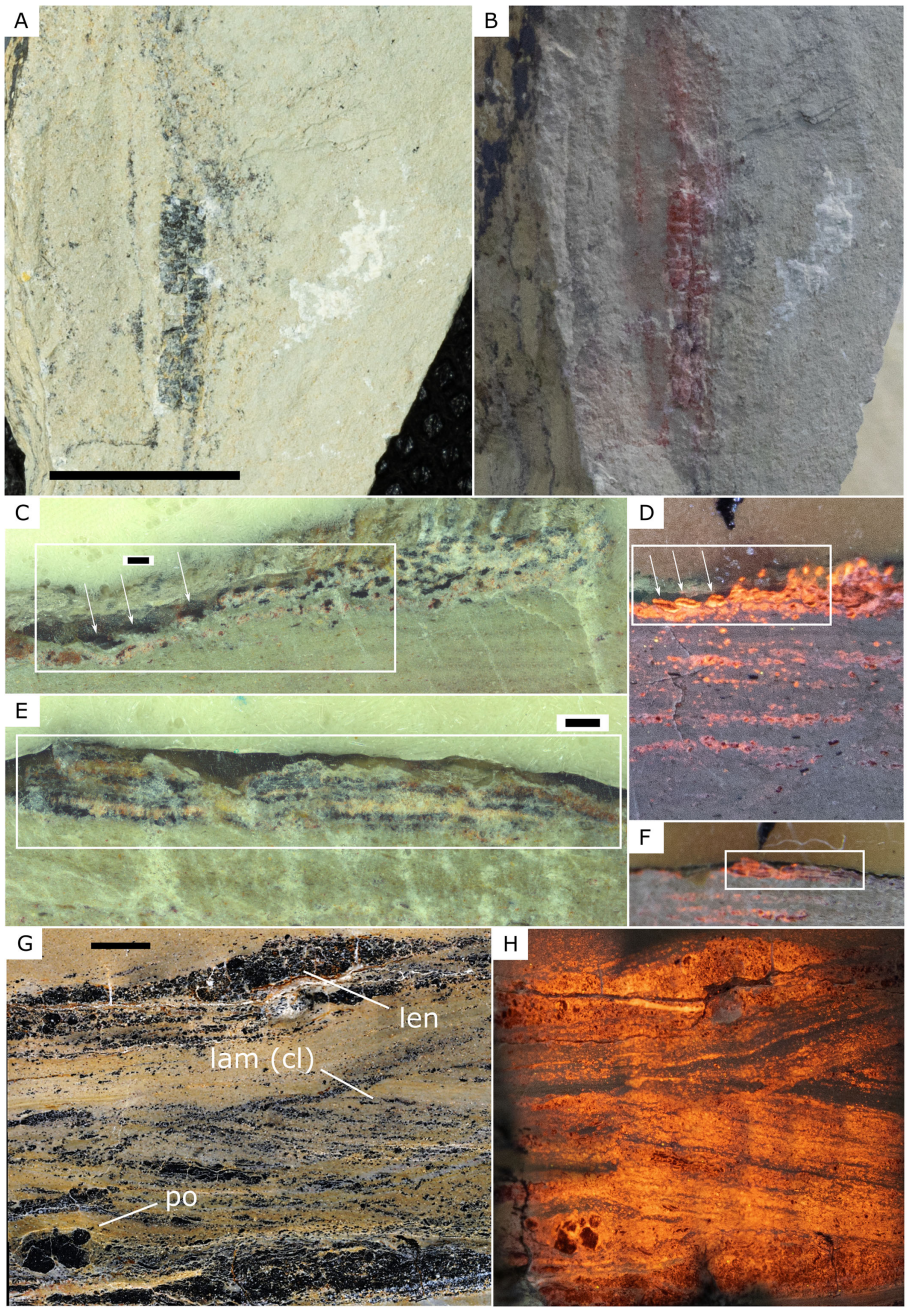

FIGURE 4
Visible light photography of fossils **(A, C, E, G)** and proton beam-induced luminescence mapping **(B, D, F, H)**. **(A, B)** *Corumbella* sample CPL/1-044. **(C, D)** *Corumbella* sample CPL/1-045A. **(E, F)** *Corumbella* sample CPL/1-045B. The pairs **(C-F)** depict rectangles delimiting the same areas, respectively. **(C, D)** are longitudinal cross-section along *Corumbella* tube. The white arrows indicate sclerites with non-luminescent cores outlined by bright luminescent margins. **(E, F)** are transverse cross-section through *Corumbella* tube. The sclerites have non-luminescent cores outlined by bright luminescent margins. The bright luminescent regions without non-luminescent cores, following the rock lamination in **(D)** and in **(F)**, represent calcite cement only. **(G, H)** Polished slab of rock. **(H)** shows that the sample is composed by clay laminae (non-luminescent laminae), carbonate (dull luminescence), and bioclasts (non-luminescent). len – lenses; lam (cl) – lamination (cross-lamination); po - pod. **(G)** was modified from Osés et al. (2025) (https://www.cambridge.org/core/journals/geological-magazine/article/clastic-sedimentary-record-impacted-by-carbonate-bioclasts-in-the-late-ediacaran/5AAD1273A34DDEA4F111B9AD1EDABBB1), published under the Copyright of CC BY 4.0 (https://creativecommons.org/licenses/by/4.0/#ref-appropriate-credit). Scale bars: **(A)** – 1 cm; **(C, D)** – 200 μm; **(G)** – 2 mm.

have gypsum (band at 1007/1008 cm^{-1}) and pyrite (Figure 9; band at 345 cm^{-1}). XRF analysis of both samples shows that mainly Fe, Cu and Zn are more abundant in the fossil from the BL facies relative to the host rock, while S, Cr, Mn, Fe, Cu, Zn and Pb are more abundant in the fossil from the GL facies in comparison to the host rock (Figure 10).

The sample GP/1E 10609 (Figures 11A–C) was radiographed with 50 kV and 79 μA, with 50 s and 70 s of integration time and 2

10.3389/fevo.2025.1669055

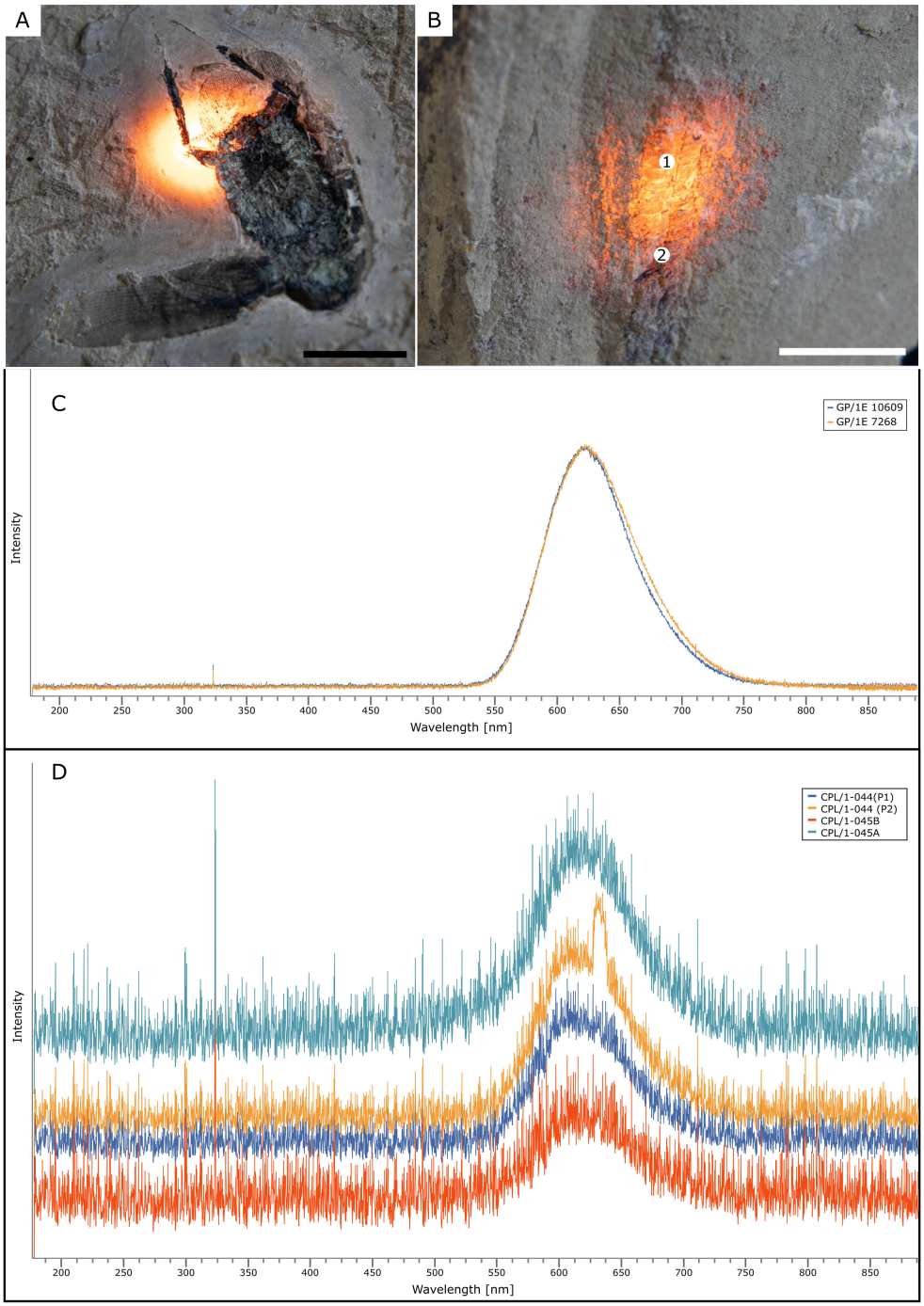

FIGURE 5
Location of points where luminescence spectra were measured and corresponding spectra. **(A)** Sample GP/1E 10609 (blattodean). **(B)** *Corumbella* sample CPL/1-044. Scale bars of **(A, B)**, respectively in Figures 3C, 4A. **(C)** Spectra of points measured in **(A)** (illuminated area) and in Figure 3B (white dot). **(D)** Spectra of points 1 and 2 measured in the *Corumbella* skeleton shown in **(B)**. Spectra of luminescent regions of samples depicted in Figure 4D (sample CPL/1-045A) and F (sample CPL/1-045B). Scale bars: **(A)** – 1 cm; **(B)** – 0.5 cm.

frames. It was not possible to observe any hidden feature in the radiographies.

The sample GP/1E 10751 (Figures 11D–G) was analysed with 50 kV and 79 μA, 2 frames, and integration time of 50 s and of 70 s. In the radiographs of this sample, no hidden anatomical features were observed, but morphological details, such as abdomen segments, are more discernible relative to optical imaging.

For sample GP/1E 10829 (Figures 11H–K), the voltage and current were set to 50 kV and to 79 μA, respectively, 2 frames were captured, and the integration time was 50 s and 70 s. The

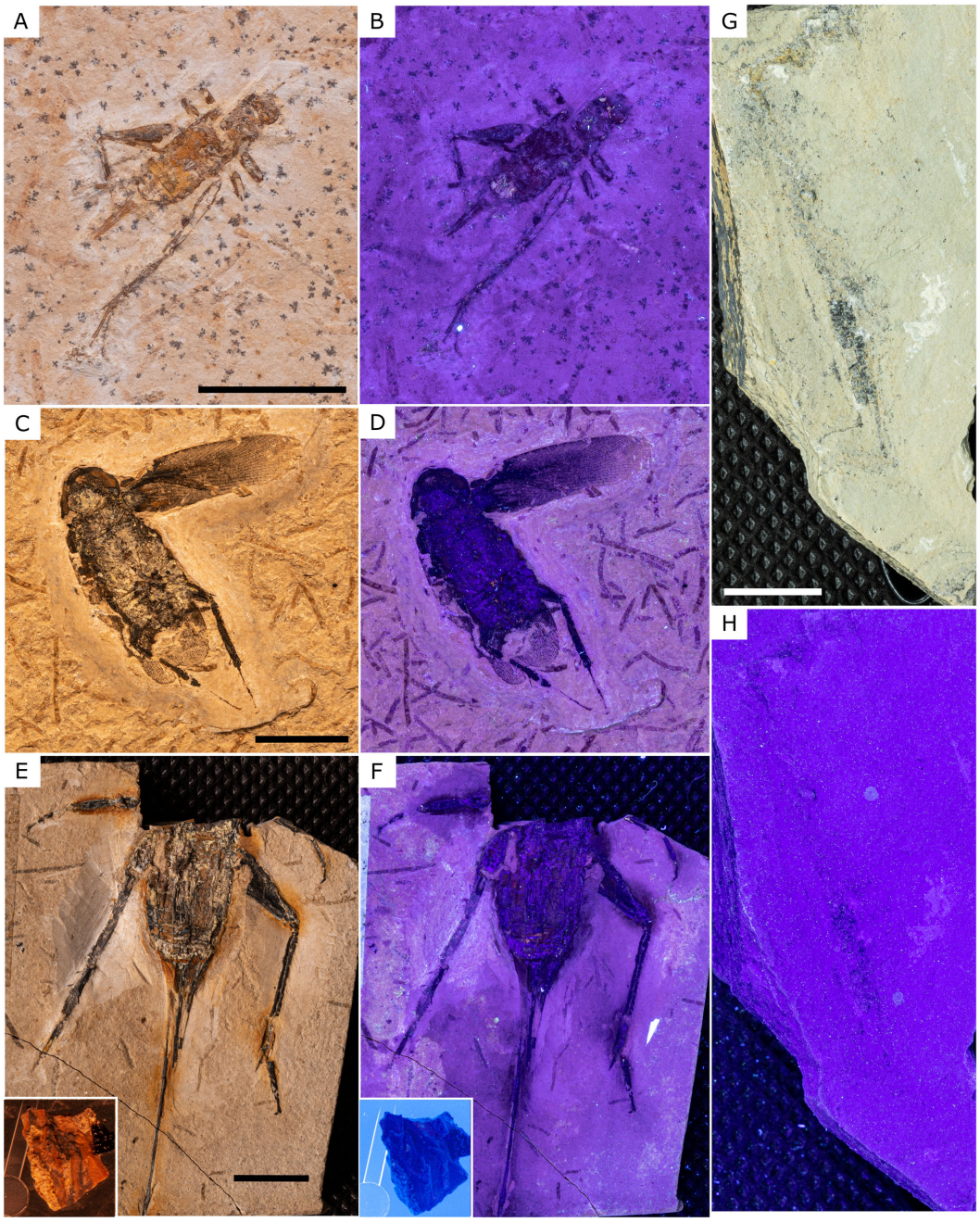

FIGURE 6
Photographs with visible light source **(A, C, E, G)** and with UV light source **(B, D, F, H)**. **(A, B)** Sample GP/1E 7268 (orthopteran). **(C, D)** Sample GP/1E 10609 (blattodean). **(E, F)** Sample GP/1E 11237C (orthopteran). **(G, H)** *Corumbella* sample CPL/1-044. The insets in **(E, F)** represent the same fragment that came apart from the right femur of the fossil specimen (see Figure 3F). Scale bars: **(A, C, E, G)** – 1 cm.

radiographs enhanced the shape of features of the head and of the thorax relative to the optical image.

The sample GP/1E 11237C (Figure 12) was imaged with voltages of 40 kV and of 50 kV, with 2 frames and current of 79 μA and of 99 μA and the integration time varied among 10 s, 70 s and 100 s. It was found that 200 s saturated the detector. The radiographs obtained with the CARESTREAM system, enhanced the contours of the body and of the legs, and revealed structures hidden in the rock and internal morphological features, neither of them visible with optical imaging (Figures 12A, C). The same sample was also imaged with 29 kV but with 220 mA•s in the MAMMOMAT 3000 Nova Siemens system, yielding a higher-quality radiography. It is possible to note a better definition of the contour of morphological structures (Figures 13A–D). A hidden portion of the abdomen appears in the radiographies (Figure 13B). Possible internal soft tissues occur inside the thorax (Figures 13B, C). The right hind femur contour is also seen uncrushed (Figures 13B, D). Internally, this femur has an array of parallel

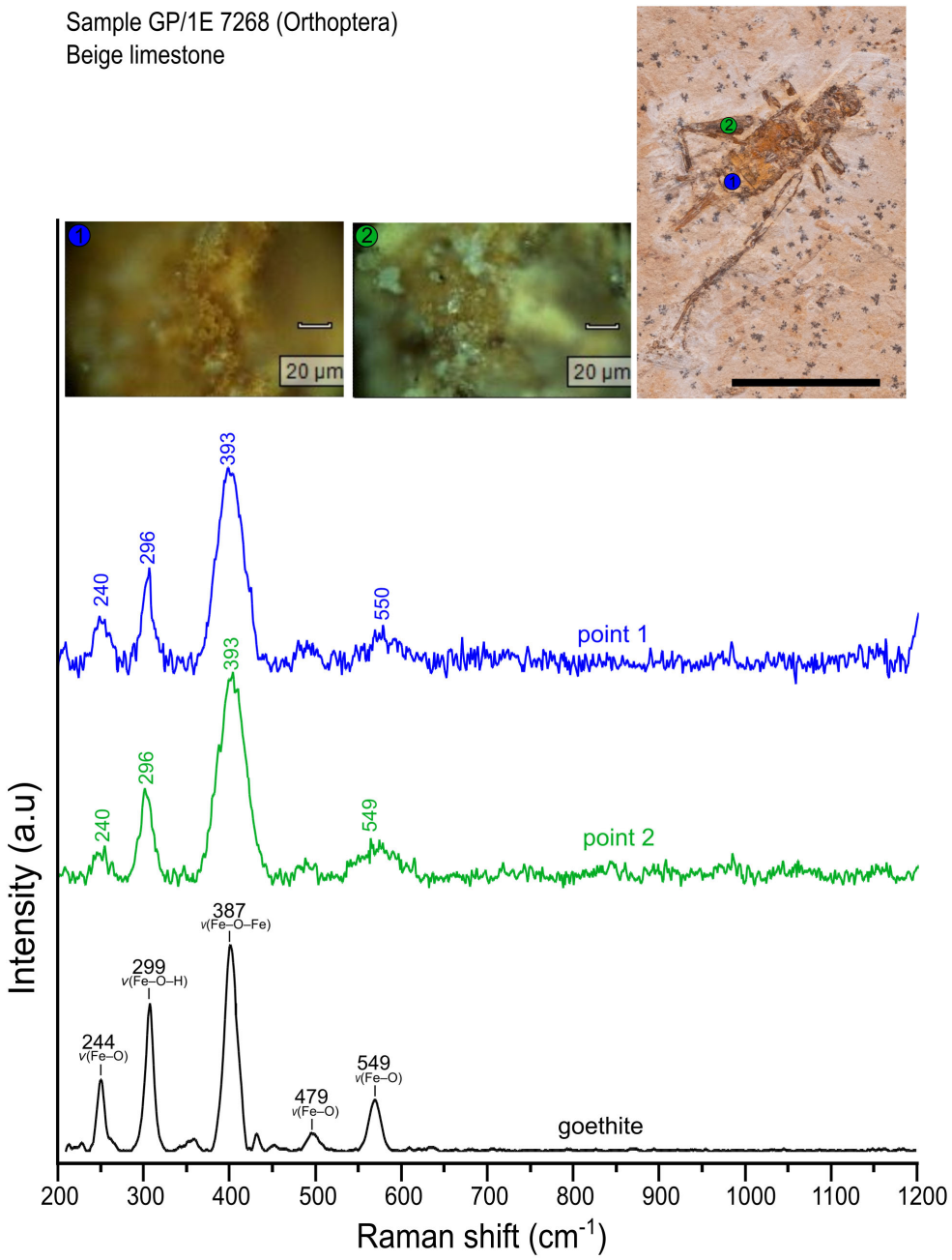

FIGURE 7
Raman spectra of sample GP/1E 7268 (orthopteran). The location of the analysed points 1 and 2 is marked as dots with different colours at the image of the fossil, and the exact points are located at the centre of the respective microscopy images. The goethite reference spectrum was used from RRUFF ID: X050091. Characteristic Raman bands of goethite are observed at 240 cm^{-1} (ν(Fe–O)), 296 cm^{-1} (δ(Fe–O–H)), 393 cm^{-1} (ν(Fe–O–Fe)), and 549–550 cm^{-1} (ν(Fe–O)), consistent with previous assignments (De Faria et al., 1997). Scale bar – 1 cm.

bands, that are aligned to the femur length, and has porous structure manifesting as a fibrous organisation (Figures 13B, D).

The sample PF 91/3485/97 (beige limestone) was analysed with 35 kV and 180 mA•s. The radiography reveals enhanced images of the contour of the head, besides structures not visible or barely visible without radiography, such as the compound eyes, the labrum and forelegs (coxa, trochanter, femur and tibia) (Figures 13E, F).

The whip scorpion GP/1E 9882 104 was imaged with 35 kV and 280 mA•s. The radiography enhances the contour of the legs and reveals hidden morphological features, such as the first pair of legs, which is hidden in the host rock, and the last pair of legs hidden under the body (Figures 13G, H).

6 Discussion

A summary of the advantages and advantages of the following discussed techniques regarding sample preparation, spatial

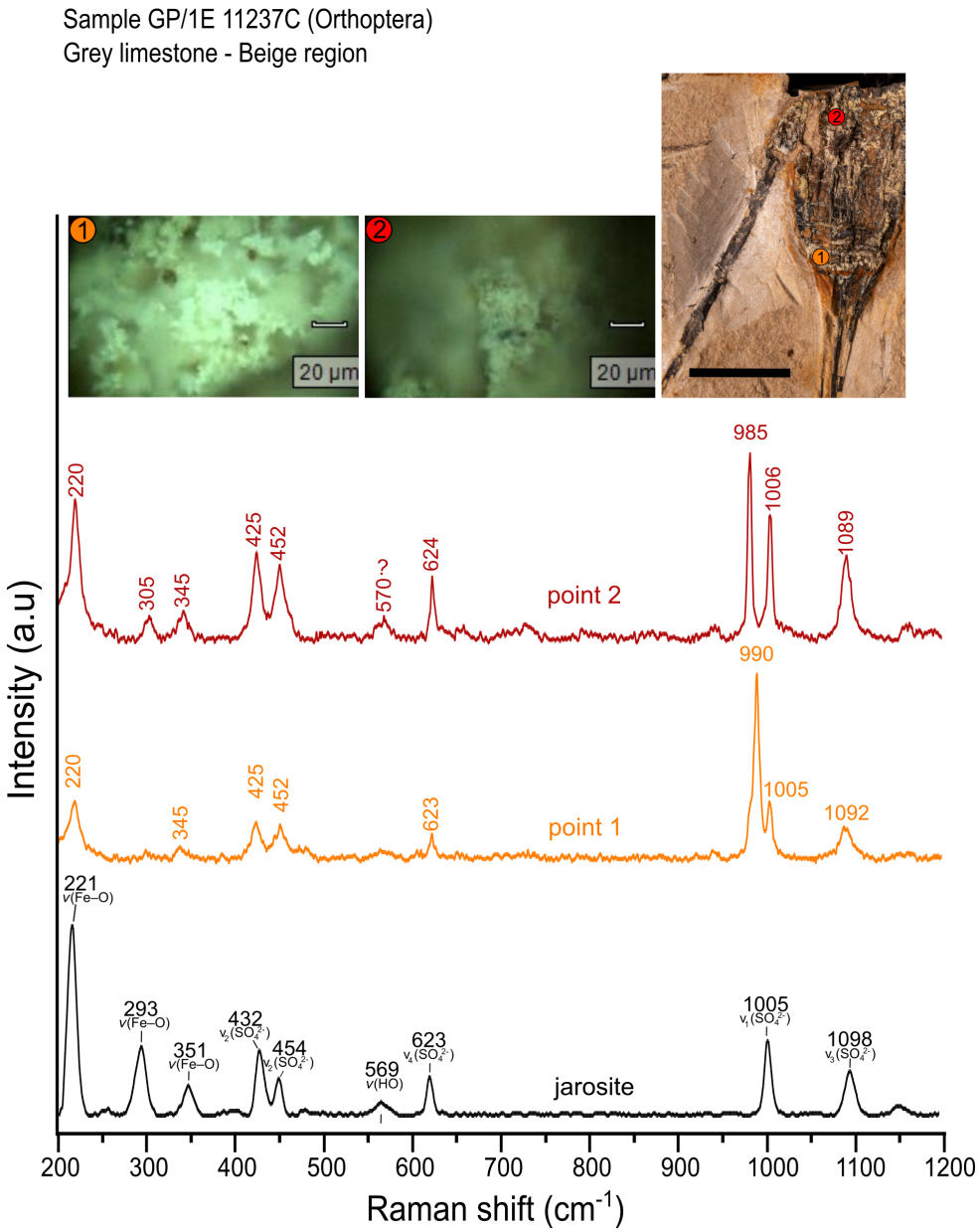

FIGURE 8
Raman spectra of sample GP/1E 11237C (orthopteran). The location of the analysed points 1 and 2 is marked as dots with different colours at the image of the fossil, and the exact points are located at the centre of the respective microscopy images. The jarosite reference spectrum was used from RRUFF ID: X050105. These are assigned to Fe–O bending (~220–305 cm^{-1}), Fe–O stretching (~345–452 cm^{-1}), δ(OH) (570 cm^{-1}), $\nu_4(SO_4^{2-})$ (~624 cm^{-1}), and to the internal modes of SO_4^{2-}: ν_1 (~990–1006 cm^{-1}) and ν_3 (~1089–1092 cm^{-1}), consistent with spectral data elsewhere (Sasaki et al., 1998; Frost et al., 2006). Scale bar – 1 cm.

resolution, analytical conditions, and imaging, can be found in Table 2.

6.1 Ionoluminescence

The IL of calcite-hosting rocks bearing non-calcite fossils, eventually with calcite infillings, enhances the contours of the morphological structures of the fossils (Figures 3B, D). The luminescence imaging of the studied samples also seems to reflect differences in the composition of the embedding host rock. The calcite-dominated host rocks BL and GL from the Crato Formation (Osés et al., 2017) have different orange luminescence responses to the interaction with the proton beam (Figure 3). The BL rock has a brighter orange luminescence (Figures 3A, B) than the GL rock (Figures 3C–F). It is possible that the higher organic matter and siliciclastic contents of GL relative to BL (Osés et al., 2017) explain such difference, as photographs were taken under the same conditions and later image processing was careful to avoid changes in IL brightness or colour. Organic matter and clay

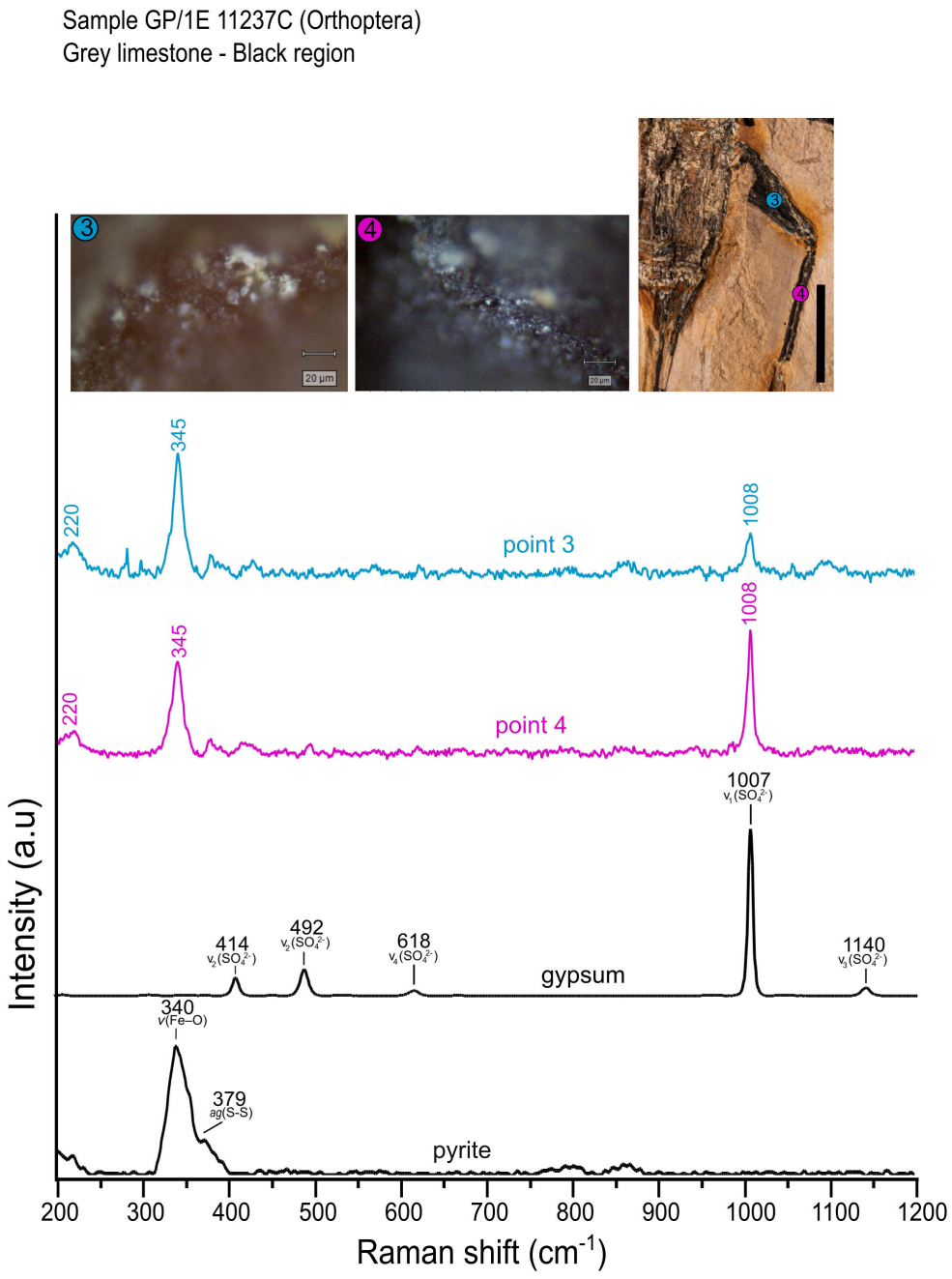

FIGURE 9
Raman spectra of sample GP/1E 11237C (orthopteran). The location of the analysed points 3 and 4 is marked as dots with different colours at the image of the fossil, and the exact points are located at the centre of the respective microscopy images. The gypsum and pyrite reference spectra were used from RRUFF ID: X050096 and R050070, respectively. Spectra from points 3 and 4 show characteristic bands of gypsum, with prominent peaks at ~1007–1008 cm^{-1} (v_1 SO_4^{2-}) consistent with sulphate group vibration in the monoclinic $CaSO_4{\cdot}2H_2O$ structure (Prasad et al., 2001) and pyrite was identified by the band at 340 cm^{-1}, assigned to the S–S stretching mode (Chen et al., 2022; Bryant et al., 2018). Scale bar – 1 cm.

minerals display variable elemental compositions depending on diagenetic processes, yielding variable luminescence (Machel, 2000), even with a non-luminescent response after stimulation with an electron beam (Osés et al., 2022). In some fossils, the calcite luminescence brightness varies from the fossil to the host rock (Figures 3B, D). This observation might be explained by variations in the elemental composition of the host rock and of the cement infilling the fossils, as different carbonate phases might change elemental composition through diagenesis (Machel, 2000).

IL can be also used to image calcite-bearing fossils embedded in host rocks of other composition (e.g., aluminosilicates). *Corumbella* from the Tamengo Fm. consists of skeletal elements called sclerites,

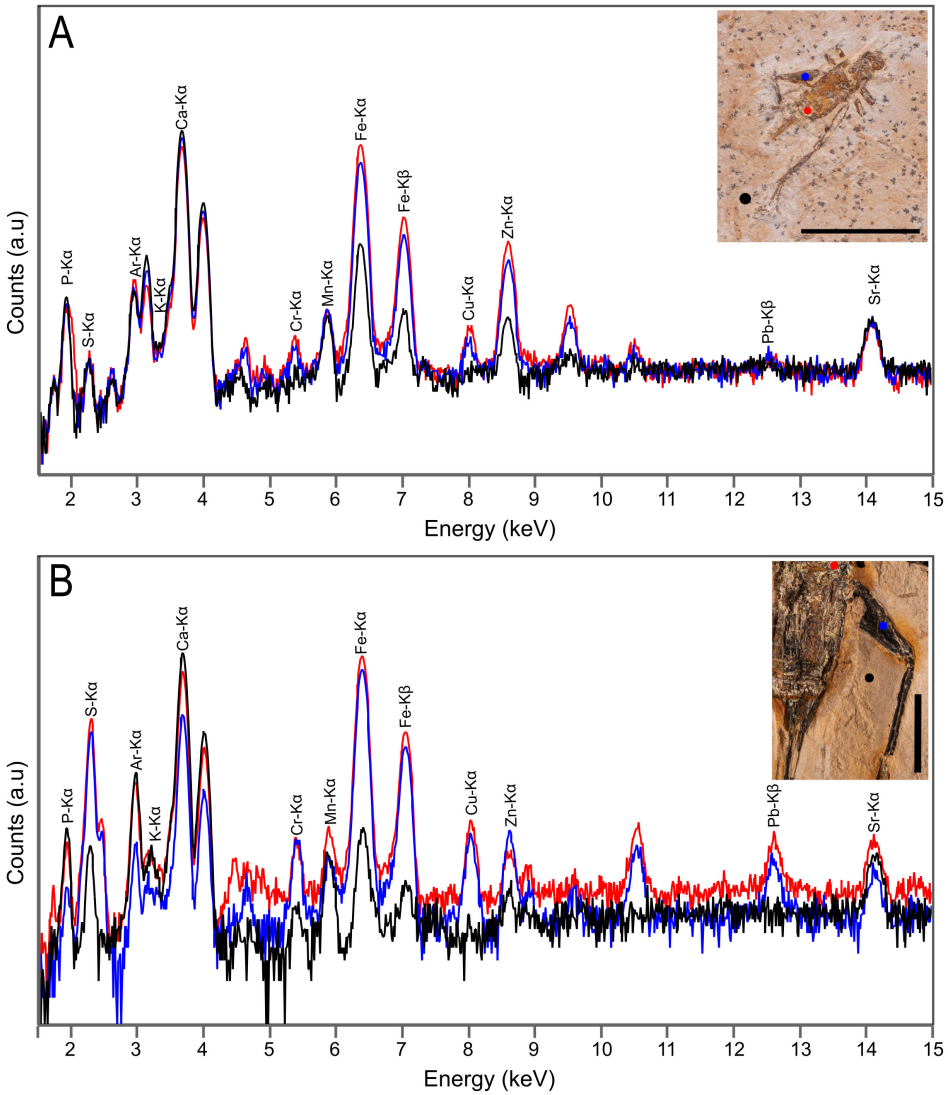

FIGURE 10
XRF spectra of samples GP/1E 7268 **(A)** and GP/1E 11237C **(B)**, both orthopterans. The location of the analysed points is marked as dots with different colours at the images of the fossils. Scale bars – 1 cm.

whose calcite composition represents recrystallisation after primary aragonite (Osés et al., 2022). Here, it is shown that the luminescence of fossils interacting with a proton beam is similar to that recorded in analyses with conventional CL, which uses an electron beam for luminescence stimulation (Osés et al., 2022). As shown by these authors, sclerites have non-luminescent cores, which are outlined by bright luminescent orange margins (Figures 4D, F). Consequently, it is possible to distinguish fossils from calcite cement, which manifests as bright luminescent regions without non-luminescent cores (calcareous fossils), following the rock lamination in Figures 4D and F. IL also enhances the contours of the sclerites, that are hardly seen under visible light (Figures 4C, D). However, IL has the advantage of enabling the imaging of totally unprepared samples (Figures 4A, B), except in cases of imaging samples internally. On the other hand, conventional CL does require sample polishing. IL of polished rock slabs bearing *Corumbella* bioclasts highlights sedimentary structures (lenses, pods, and cross-lamination) formed by bioclasts (calcareous fossil fragments), clay minerals and carbonate (Figures 4G, H). Osés et al. (2025) proposed that the multi-element construction of the *Corumbella* skeleton (Osés et al., 2022) favoured its disarticulation and fragmentation, thus yielding a carbonate sedimentary source. These bioclasts, when interacting with sedimentary dynamics in a fine siliciclastic sediment enabled the formation of sedimentary structures, and consequently the record of local sedimentary conditions (Osés et al., 2025). Here, IL imaging of a sample analysed by these authors (Figure 4H) highlights these sedimentary structures and the contribution of a carbonate phase, besides the bioclasts.

Luminescence wavelength reflects crystal coordination number (that is the number of ions surrounding a differently charged ion in a crystal lattice), explaining bright orange luminescence of calcite

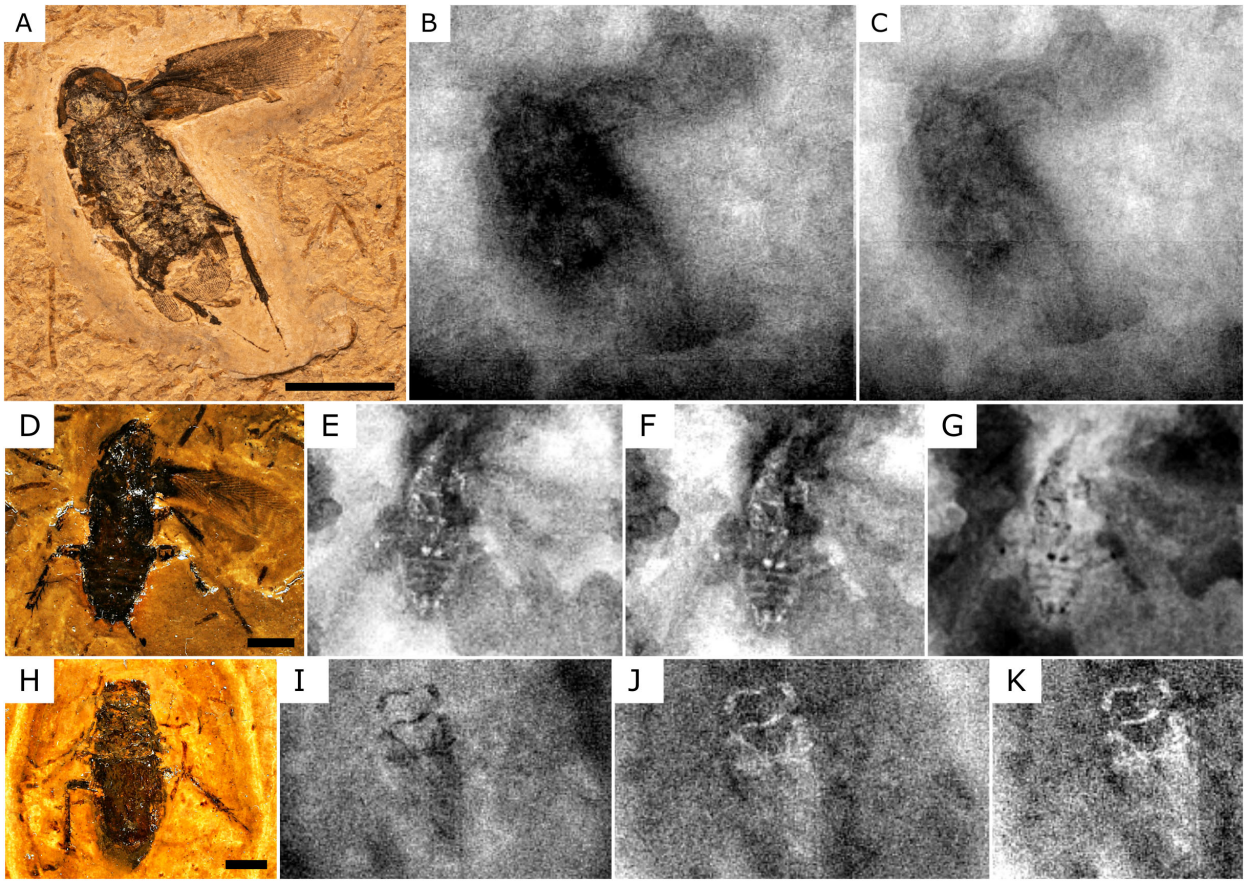

FIGURE 11
Radiography of blattodea samples GP/1E 10609 **(A–C)**, GP/1E 10751 **(D–G)**, and GP/1E 10829 **(H–K)**. Analyses were made using the CARESTREAM system. **(A)** Visible light photography of sample GP/1E 10609. Scale bar in **(A)** – 1 cm. **(B)** Radiography performed using 50 kV, 79 μA, 50 s of integration time and 2 frames. **(C)** Radiography performed using 50 kV, 79 μA, 70 s of integration time and 2 frames. **(D)** Visible light photography of sample GP/1E 10751. Scale bar in **(D)** – 5 mm. **(E)** Radiography performed using 50 kV, 79 μA, 50 s of integration time and 2 frames. **(F, G)** Radiography performed with 50 kV, 79 μA, 70 s of integration time and 2 frames. **(F, G)** were processed with different colour backgrounds (white and black, respectively). **(H)** Visible light photography of sample GP/1E 10829. Scale bar in **(H)** – 5 mm. **(I, J)** Radiography performed using 50 kV, 79 μA, 50 s of integration time and 2 frames. **(I, J)** were processed with different colour backgrounds (white and black, respectively). **(K)** Radiography performed with 50 kV, 79 μA, 70 s of integration time and 2 frames.

with Mn^{2+} ions (octahedral coordination number; Yang et al., 1994). Mn^{2+} acts as a luminescence activator, in other words, it is a secondary ion excited by another ion (coactivator) that enhances its luminescence (Yang et al., 1994). This explains the luminescence orange colour observed in the analysed samples (Figures 3, 4). Activators are defined as trace elements with an equivalent valence state that occur at specific positions of the crystal lattice of a mineral (Machel, 2000). EDXRF data showed the occurrence of Mn in the host rock of the Crato Fm. insects (Osés et al., 2016), while EPMA of *Corumbella* skeletons indicated increasing of CL brightness with elevated Mn concentration towards the margin of the sclerites (Osés et al., 2022). The core of *Corumbella* fossils is non-luminescent, which is explained by the lower concentration of Mn^{2+} relative to their margin (Figures 4D, F; Osés et al., 2022). Additionally, the organic matter content of the fossils (Osés et al., 2022) might also explain this luminescence response, depending on the accumulation of quenching elements during diagenesis (Machel, 2000). Considering the previous discussion, carbonate fossils embedded in carbonate host rocks could potentially be distinguished from each other if their elemental composition/concentration is different.

On the other hand, some ions act as quenchers (e.g., Fe^{2+} and Fe^{3+}), inhibiting luminescence of other ions (Machel, 2000; Šoster et al., 2023; Sasan et al., 2022). This quenching effect in luminescence by both Fe^{2+} and Fe^{3+} is observed in the non-luminescent fossil insects (Figure 3B), which are composed by goethite (Fe^{3+}) in the BL facies from the Crato Fm. (Figure 7; Osés et al., 2016). Spectroscopic data for fossil insects from the GL facies from the Crato Fm. show that they are composed by pyrite (Fe^{2+}) and by jarosite (Fe^{3+}) (Figures 8, 9), thus explaining their non-luminescent aspect (Figures 3D, F).

The luminescence spectra of regions with host rock (mainly)/fossil of samples GP/1E 7268 and GP/1E 10609, which are different samples, representative of distinct facies from the Crato Fm. (respectively, BL and GL) have a strong broad peak centred in ca. 622 nm (Figures 5A, C). The transitions of electrons of specific elements associated with de-excitation of higher-energy states to

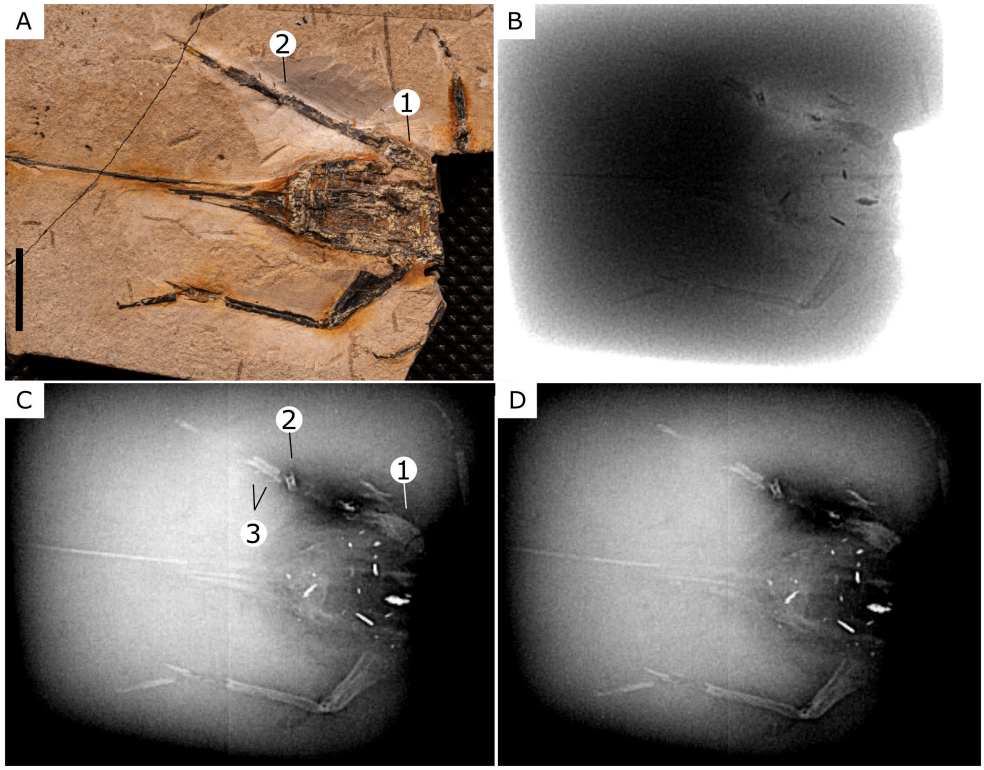

FIGURE 12
Radiography of sample GP/1E 11237C (orthopteran). The analyses were made using the CARESTREAM system. **(A)** Visible light photography. Scale bar in A – 1 cm. **(B)** Radiography performed with 40 kV, 99 μA, 10 s of integration time and 2 frames. **(C)** Radiography performed with 50 kV, 79 μA, 100 s of integration time and 2 frames. **(D)** Radiography performed with 50 kV, 79 μA, 70 s of integration time and 2 frames. Numbers in **(A, C)** explained: 1-External view of femur **(A)** and internal morphology **(C)**; 2-Apparently well-preserved leg **(A)** and radiography showing leg fragmentation **(C)**; 3-Leg spines are observed in radiography only **(C)**.

ground level energy have specific wavelengths. The wavelength of 620 nm was reported as representing transitions between the T_{1g} to the A_{1g} states of Mn^{2+} in calcite (Pedone et al., 1990; Romppanen et al., 2021 and references therein). This broad band hampers the observation of emission bands that characterise the presence of other trace elements in calcite, like Sm and Eu (Romppanen et al., 2021). The luminescence spectral characterisation for *Corumbella* fossils showed a strong broad peak centred in ca. 615 nm and another one in ca. 631 nm (the latter peak in one measurement only) (Figures 5B, D). These peaks can be also attributed to the Mn^{2+} luminescence, which are related to the transition $^4T_{1g} \rightarrow {}^6A_{1g}$ (El Ali et al., 1993 and references therein; Yang et al., 1994; Kusano et al., 2014 and references therein).

IL and optical microscopy-based CL (OMCL) enable the visualisation of luminescence colours, whose images are collected through an optical petrographic microscope with a camera in the later technique. CL colour visualisation can be switched to visible light imaging, both not possible in SEM-based CL (SEMCL) systems (Boggs and Krinsley, 2006). IL and OMCL do not require sample coating, which is needed for SEMCL to avoid the accumulation of electron charges in non-conductive minerals (Boggs and Krinsley, 2006). OMCL and, especially SEMCL, enable high magnification and thus higher spatial resolution imaging (Boggs and Krinsley, 2006). Regarding the LAMFI, the spot size at the beamline exit is of ca. 1 mm^2, which may demand greater increments of targeted areas. Limited magnification in IL workstations can be overcome by using appropriate camera lenses, endoscopic cameras or even microscopes.

OMCL and SEMCL usually require the preparation of highly-polished thin sections or resin-embedded samples, thus potentially destroying samples. The analysis is made using high magnifications, requiring smooth surfaces, and the electron beam operation requires vacuum conditions, which limits sample size as it should fit commonly small vacuum chambers. Epoxy resins employed in thin-section preparation can be luminescent, which may affect CL analyses (Boggs and Krinsley, 2006). Though the access to some accelerator facilities may require a specific process, others grant access following schemes of OMCL and SEMCL laboratories. Some advantage of the IL mapping method here employed are that it enables imaging of samples of a wide size and weight range, that are limited to the capacities of the motorised sample holder only, do not require any previous preparation, and do not need to fit vacuum chambers, as analyses are conducted in air condition. EBSD (electron backscattered diffraction) requires high polishing, that cannot be applicable to fragile samples in thin sections. Then, the preparation of samples embedded in resin blocks is preferable. These can be analysed in just a few conventional CL systems, that allow electron beam reflection (e.g., Osés et al., 2022), but can be analysed with IL (Figures 4C–F), which then permits more flexible sample preparation techniques for EBSD.

10.3389/fevo.2025.1669055

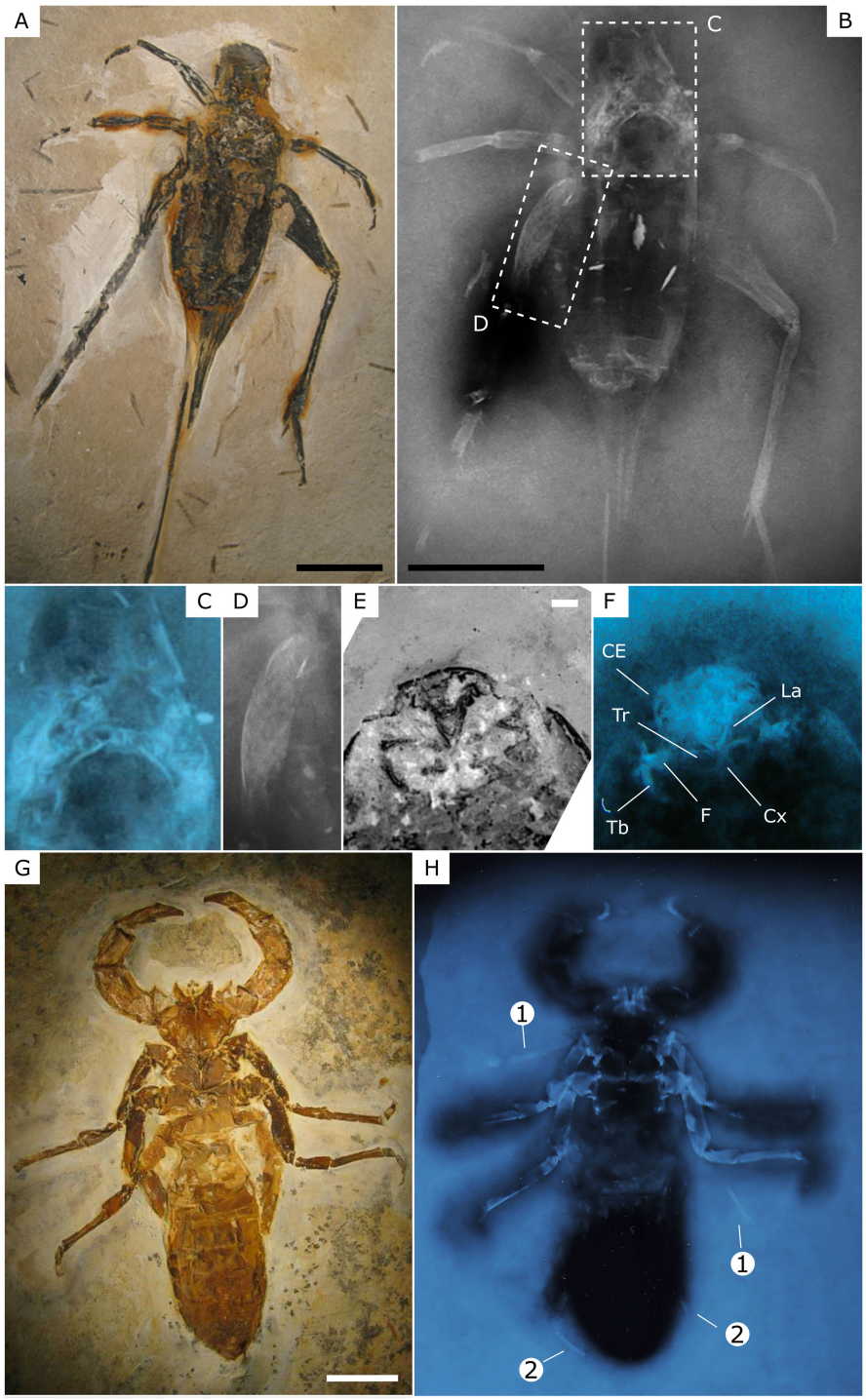

FIGURE 13
Radiographies of samples using the MAMMOMAT 3000 Nova Siemens system. **(A)** Visible light photography of sample GP/1E 11237C (orthopteran). **(B)** Radiography of sample in **(A)**. **(C, D)** Areas delimited by dashed rectangles in **(B)** showing morphological features not visible in light photography [**(C)** – possible soft tissues inside the thorax; **(D)** – possible muscle fibres inside the femur]. **(E)** Visible light photography of sample PF 91/3485/97 (heteropteran). **(F)** Radiography of sample in **(E)**. La-Labrum. Cx-Coxa. Tr-Trocanther. F-Femur. Tb-Tibia. CE-Compound eyes. **(G)** Visible light photography of sample GP/1E 9882 (Uropygi). **(H)** Radiography of sample in **(G)**. The numbers 1 and 2 respectively indicate the first pair of legs and the last pair of legs, which are visible in the radiography only. Scale bars: **(A, B, G)** - 1 cm **(E)** – 1 mm.

TABLE 2 Advantages and disadvantages of compared techniques.

Analytical technique	Sample preparation		Spatial resolution		Analytical conditions		Image produced	
	Advantages	Disadvantages	Advantages	Disadvantages	Advantages	Disadvantages	Advantages	Disadvantages
Ionoluminescence (IL)	Only required to enable access to the interior of samples; no coating is required		Minimum beam size of ca. 1 mm^2	Limitation in the magnification - can be overcome by the type of photography system	Operation in air condition permits flexible sample sizes; samples are not analysed by beam transmission, which avoids sectioning and polishing of fragile samples; lower current values and greater volume of interaction than OMCL reduce beam damage; spectral acquisition and PIXE measurements	Beam can cause damage to organic-rich samples	Visible light and luminescence colours	
Optical microscopy-based CL (OMCL)	No coating is required	High-polished thin sections or resin embedded sections; sample destruction; epoxy resins may be luminescent	The limit is the magnification of the microscope lenses			Vaccum operation chambers limit sample size; higher current values and shallower volume of interaction than IL may cause beam damage	Visible light and luminescence colours	
SEM-based CL (SEMCL)		High-polished thin sections or resin embedded sections; sample destruction; epoxy resins may be luminescent	Beam size in the order of microns			Vaccum operation chambers limit sample size; higher current values and shallower volume of interaction than IL may cause beam damage		Visible light and luminescence colours are not depicted
UV fluorescence photography (UVF)	No preparation is required		The limit is the magnification					
Radiography	No preparation is required			The type of sensor				
X-ray fluorescence (XRF)	No preparation is required		Minimum beam size of 1 mm		Non-invasive			
Raman micro-spectroscopy (μRS)	No preparation is required		Minimum beam size in the order of microns			Laser beam can cause damage		

10.3389/fevo.2025.1669055

Due to beam energy being in the MeV range (relative to keV of an electron beam), IL has the capacity of exciting higher electronic levels. Relative to CL, beam damage is reduced, as current values are lower and beam penetration is higher than an electron beam (more than 10 μm of protons interacting with inorganic solids) (Calderon, 2008; Castillo et al., 2008; Yang et al., 1994), though there may be beam damage in organic-rich samples even with lower currents. In the LAMFI setup, besides IL imaging and spectral acquisition, the same luminescent spot can be analysed using PIXE, which can be used to complement spectral information, giving its higher sensitivity for trace element identification relative to EPMA, commonly integrated with CL (Yang et al., 1994; Calderon, 2008), and occasionally even being coupled to spectrometers (Boggs and Krinsley, 2006). Though usually employed as point measurements, PIXE can be performed over an area yielding a 2D elemental map (Osés et al., 2016; Silva et al., 2018), which can be compared to the respective IL mapping, thus increasing the representativeness of the sample analysis. This combination of techniques would resolve some drawbacks of CL, like the understanding of the elements causing luminescence, enabling the test of diagenetic alteration of carbonates (England et al., 2006).

6.2 UV fluorescence, XRF and micro-RS

The UVF technique enabled us to note heterogeneities in the fluorescence of some samples, which guided spectroscopic analyses, as suggested by Riquelme et al. (2009). The incidence of UV light at fossil insects yields dark brown fluorescence of originally dark regions (Figures 6A–F). Micro-RS analyses indicate that these regions are mainly composed by either iron oxy-/hydroxides (goethite; Figure 7), or by pyrite and gypsum (Figure 9), respectively in fossils from the BL and the GL facies. As also indicated by these authors, EDXRF data supports these mineralogies, given the high abundance of Fe in the BL fossils, and of Fe, S, and Ca in the GL fossils (Figure 10).

The white/beige mineral phase in the GL fossils have a bright purple/bluish fluorescence (Figures 6C–F). This material occurs inside the fossils (Figures 6C–F), notably in a hind femur of the specimen GP/1E 11237C (Figures 6E, F, insets). It is not possible to observe the white/beige material, nor any structure formed by it externally (Figure 13), but only after sample preparation (Figures 6E, F) and, interestingly, by previous radiography characterisation of the sample (Figures 12C; 13B, D). In these radiographies, it is possible to note that the white/beige phase manifests a fibrous morphology, which likely represents muscular soft tissues. The white/beige phase has a granular habit (Figure 8) and is composed by jarosite, as shown by micro-RS characterisation (Figure 8). EDXRF data supports this composition, as evidenced by the occurrence of Fe and S (Figure 10).

Fe^{2+} and, potentially, Co^{2+} and Ni^{2+} act as quenchers in pyrite (Machel, 2000) and in other sulphides like sphalerite (Šoster et al., 2023), and Fe^{3+} is also a quencher of luminescence (Sasan et al., 2022), thus explaining the dark colour of both pyrite-rich and goethite-bearing regions in the studied fossil insects under UV light (Figures 6B, D, F). Jarosite is efficient in blocking UV transmission, which has made it promising for targeting extra-terrestrial materials with astrobiological importance (Carrier et al., 2019 and references therein). Jarosite-rich substrates irradiated with longer UVA/UVB radiation (which is our case) diminishes even more efficiently light transmittance and can potentially increase UV reflectance (Carrier et al., 2019).

The association of these sulphates within the fossils, in which they preserve soft tissues, represent novelties for the fossilisation of fossil insects from the Crato Fm. Previous works showed that the dark insects found in the GL facies are preserved by kerogen (Bezerra et al., 2018; Dias and Carvalho, 2022), thus following the pyritisation-kerogenisation model proposed by Osés et al. (2017) for fishes and later confirmed by Bezerra et al. (2018) for insects. Our new data urge for the development of a more complex preservation model than previously assumed for the Crato Fm. insects.

Corumbella skeleton does not fluoresce when irradiated by UV light (Figure 6H). These fossils are constituted by calcite with organic matter contribution and are enveloped by an iron oxy-/hydroxide film (Osés et al., 2022). This composition may explain the non-fluorescent response to UV light. Feng et al. (2021) proposed that Fe^{3+} incorporation to carbon substrates quenches organics fluorescence due to a filtering effect caused by this ion, which absorbs UV.

Ion beam stimulated luminescence of carbonate in *Corumbella* skeletons (Figures 4, 5), but the lack of visible fluorescence induced by UV light (Figure 6H) may be explained by the selective interplay of quenchers and activators relating to different wavelengths and thus emission energies (Boggs and Krinsley, 2006). In particular, ion beams are more effective in activating luminescence centres, thus yielding luminescence, while UV absorption may be prevented depending on the material or the activation of luminescence centres may not occur depending on the energy of the UV radiation source.

This work represents an advancement in the characterisation of sulphides, sulphates and iron hydroxides in fossils by UV light. Previous research has focused on the characterisation of phosphatised (Haug et al., 2009; Riquelme et al., 2009; Hone et al., 2010; Tischlinger and Arratia, 2013; Crippa and Masini, 2022), silicified/aluminosilicified (Frese et al., 2017), carbonate (Crippa and Masini, 2022) and carbonaceous compressions (Boderau et al., 2024). We show that the integration of UVF with XRF and RS enables disentangling mixed mineral signals with imaging and spectroscopic techniques, which may be a challenging task for taphonomy and astrobiology (Liu et al., 2020).

6.3 Radiographies

It is possible to notice in the images that the contours and details of the fossil structures are better defined in the radiographs than in the visual analysis of the specimens (Figures 11–13). Hidden structures are observed within the host rock, such as leg spines and a fragmented leg in an orthopteran (Figures 12A, C), forelegs of a

hemipteran (Figures 13E, F), and fore-/hindlegs of an arachnid (Figures 13G, H). In other cases, internal morphology is also observed. An indistinct mass within the thorax of an orthopteran (Figures 13B, C) likely represents soft tissues, as similarly shown by Grimaldi (2005) and by Heads and Martins-Neto (2007). Notably, fibrous structures organised in a network likely representing muscular tissue occur inside the leg of this orthopteran (Figures 13B, D). These features were later exposed, enabling direct assessment by imaging techniques (Figures 6E, F). Morphological structures observed in these radiographies, but not in the unexposed original sample, may have taxonomic implications. The radiograph of sample PF 91/3485/97 reveals the forelegs of the specimen (Figures 13E, F). They have enlarged forefemura and curvilinear anterior tibiae, which suggest the placement of this specimen in the family Naucoridae (Heteroptera, Hemiptera) (Sites, 2022).

The details observed in the radiographies of Figures 11 and 12 were recorded due to differences in the radiodensity contrast of different minerals that build up the samples. Contrast is a central concept in radiographic imaging, being defined as the difference in brightness among regions forming the analysed object (Williams et al., 2007). Radiodensity is proportional to attenuation (radiation intensity loss) or absorption differences of materials, thus being proportional to the density of compounds, to the atomic number of elements forming them, and to the thickness of the object (Lang and Middleton, 2005; Williams et al., 2007; Tompe and Sargar, 2022) – denser materials absorb more radiation yielding brighter images (Curry et al., 1990; Langland et al., 2002; Bushberg et al., 2011; White and Pharoah, 2013). The host rock of the Crato Fm. samples is mainly made of calcite (d=2.71 g/cm^3), while the exoskeleton of insects (and arachnids) is replicated by iron oxy-/hydroxides, like goethite (d=4.27 - 4.29 g/cm^3) or pyrite (d=4.8–5.0 g/cm^3) and subordinated gypsum (d=2.31 - 2.32 g/cm^3); and internal parts (including soft tissues) have jarosite (d= 2.9 - 3.26 g/cm^3), gypsum, and possibly pyrite. The measured densities are available at *mindat.org* website. These values indicate that there is not any overlap of densities of minerals occurring in samples of a single type of preservation, which accounts for the discrimination of hidden features in the host rock and inside the fossils.

The application of different radiography techniques, with systematic variation of parameters, but maintaining constant tube-sample distance (41 cm) and number of frames (2), allowed the establishment of the best experimental conditions for analysing samples of Crato Fm. fossil arthropods and, consequently, samples from other geological units with similar compositions. The best results for the portable X-ray tube were obtained using high parameter values (high voltage and current) and less thick samples. Some very thick samples (for example, ≥ 2 cm) block X-rays, preventing them to be captured by the digital detector. It was found that the ideal thickness for carrying out the measurements is up to 1 cm using the conditions presented here (Table 1). For thicker samples, more energy (voltage and current) would need to be used.

Higher voltage tubes produce higher-energy X-rays with greater penetrability, increasing photons reaching the detector, which yields better signal-to-noise ratio. Higher-energy photons are less absorbed, leading to lower contrast, which alters image quality (McCollough, 1997; Schueler, 1998; Lang and Middleton, 2005; Williams et al., 2007; Tompe and Sargar, 2022).

Comparing the radiographs resulting from different integration times, while voltage and current are kept constant, it is noticeable that image quality increases along with longer acquisitions (Lang and Middleton, 2005). The morphology of the fossils GP/1E 10609, GP/1E 10751 and GP/1E 10829 are more defined with 70 s of integration time (Figures 11C, F, G, K) relative to measurements during 50 s (Figures 11B, E, J). Integration time is directly proportional to the sample's exposure time to radiation (Lang and Middleton, 2005) (Equation 1). The number of frames that will be captured represents an accumulation of measurements that enhances image quality. Higher exposure (current values and exposure time) yields high signal-to-noise ratio (SNR) in the detector as more photons reach it, thus increasing image quality (Tompe and Sargar, 2022).

$$Exposure \propto I \star T \tag{1}$$

where "exposure" is the result of the product between the current (I) and the integration time (T) (Zangerl, 1965; Schueler, 1998; Lang and Middleton, 2005).

The greater the current, there will be a more intense flow of electrical charges in the tube, increasing the intensity of the X-rays, that is the number of photons that reach the target. Increasing the current allows lower acquisition time of radiographies (Equation 1), but it also decreases the contrast of the image, thus affecting its quality (McCollough, 1997; Lang and Middleton, 2005; Tonnessen and Pounds, 2011; Huda and Abrahams, 2015; Sy et al., 2022).

In relation to the fossil GP/1E 11237C, an increase in integration time and in voltage yielded greater sharpness of morphology (contours of the body, legs and preserved internal soft tissues), despite a decrease in current (Figures 12B, C). The relationship among radiation intensity, voltage, current and geometric arrangements is given by the Equation 2. Therefore, increasing the voltage a little yield a significant difference in the emitted X-rays and thus in the final image, even that the current is decreased. Equation 1 explains the decrease in image sharpness when integration time was lowered from 100 s to 70 s (Figures 12C, D) (Lang and Middleton, 2005). Equation 2 also shows how intensity decreases with higher distances between the tube and the sample.

$$Intensity \propto I \frac{V^2}{D^2} \tag{2}$$

where I is the electric current, V^2 is the voltage raised to power 2 and D^2 is the distance between the tube and the sample raised to power 2 (Zangerl, 1965; Lang and Middleton, 2005).

Interestingly, radiography using the MAMMOMAT 3000 Nova equipment yielded sharper images of the sample GP/1E 11237C (Figures 13B–D). This can be explained by the quality of the radiation sensitive film relative to the digital detection system used in the LACAPC system (Lang and Middleton, 2005).

Changing this distance between the X-ray tube and the targeted object causes variations in the imaged area of the object, that is

magnification. If the tube is close to the object, the image will be enlarged, facilitating the visualisation of finer structures (Tompe and Sargar, 2022). Furthermore, the distance between the X-ray tube and the object controls distortion and the radiation dose, as the distance is inversely proportional to the image distortion and directly proportional to the amount of integration time. The fossils were placed directly over the detector, thus minimizing image unsharpness (Lang and Middleton, 2005), according to Equation 3. Additionally, "*a*" was greater for the MAMMOMAT 3000 Nova than for the LACAPC system. Moreover, the former has a focal spot size "*S*" of 0.1 mm, which is smaller than the focal spot size of the X-ray tube used in the LACAPC system. Consequently, Equation 3 explains the greater sharpness (low "U_g") of analyses made using the MAMMOMAT 3000 Nova system. Indeed, radiographic image quality also depends on spatial resolution, that describes how possible is to distinguish adjacent features in an image, which relies on magnification, *S*, and detector resolution (Williams et al., 2007; Tompe and Sargar, 2022).

$$U_g = \frac{S \star b}{a} \quad (3)$$

where U_g represents the geometric unsharpness (lack of sharpness), *S* the focal spot, *b* is the distance between the sample and the detector (digital or radiation sensitive film) and *a* is the distance between the X-ray tube and the object (Lang and Middleton, 2005).

7 Conclusions

Here, we combine imaging and spectroscopy techniques to understand fossilisation processes, we develop a method of IL image mapping and processing in the LAMFI external beamline aiming the characterisation of palaeontological samples, and establish radiography parameters for analysing fossils from the Crato Fm.

The combined application of different palaeometric techniques was important to the characterisation of arthropod fossils from the Cretaceous and of the Ediacaran metazoan *Corumbella*. The development of the mapping method for the application of IL with a proton beam in the LAMFI laboratory proved to be remarkable for imaging the luminescence of rocks and fossils, not only composed by calcite, but potentially of other mineralogical compositions too. In this case, the palaeometry branch of method development enabled advantages for the morphological and compositional characterisation of fossils and rocks, in comparison with other currently used techniques. IL analyses do not require vacuum operation nor, eventually, sample preparation that may cause damage, as it occurs in CL. Moreover, it operates with lower currents and the beam has a greater penetration, thus mitigating beam damage involved in CL. The vantage of using a spectrophotometer and PIXE in combination with IL in the LAMFI external beam is paramount for the determination of elements that cause luminescence in palaeontological/geological materials.

The imaging of fossils with UV light sources proved to be relevant to the initial characterisation and screening of samples, as it revealed varied fluorescence responses depending on the mineralogy of these samples, as shown by independent EDXRF and micro-RS characterisations. The insects from the Crato Formation that are preserved by iron oxy-/hydroxides in the BL facies do not show a distinct fluorescence. However, samples from the GL facies have dark regions and more constrained, internal, regions and soft tissues with a vivid purple fluorescence, respectively with pyrite/gypsum and jarosite composition predominantly. These results yield more complexity to the preservation of fossils from the Crato Formation. This is an example of how the palaeometric approach of progressively using complementary techniques, with independent physical and chemical principles, is crucial to the investigation of fossilisation. IL and UVF are complementary in the analysis of the luminescence of fossils. This approach is still underexplored by the palaeontological community, which would greatly benefit from a more integrated characterisation of fossils in taphonomic studies.

Radiography of arthropods from the Crato Formation using different techniques has proven to be an efficient non-destructive approach that enhanced the morphology of the fossils and showed morphological features hidden by the host rock, which altogether enable taxonomic refinement. Radiography also revealed the internal anatomy of preserved soft tissues in an orthopteran sample. These structures variations were captured due to differences in the composition of the fossils, as supported by independent imaging and spectroscopic analyses. This approach reinforces the explanatory power of integrative characterisation of fossils. The test of parameters using different systems provides a toolkit to researchers who aim to analyse samples of similar composition with radiography, thus optimising their decisions for fossil preparation and screening of samples for further investigation.

Data availability statement

The original contributions presented in the study are included in the article/Supplementary Material. Further inquiries can be directed to the corresponding author.

Author contributions

GO: Investigation, Writing – original draft, Writing – review & editing, Methodology, Resources, Conceptualization, Formal analysis, Funding acquisition, Validation. SB: Methodology, Validation, Investigation, Writing – review & editing, Formal analysis. SL: Investigation, Writing – review & editing, Formal analysis, Validation, Methodology. TuS: Validation, Investigation, Formal analysis, Methodology, Writing – review & editing. CR: Investigation, Methodology, Validation, Writing – review & editing, Formal analysis. GP: Writing – review & editing, Validation. JD: Validation, Writing – review & editing. IC: Writing – review & editing, Validation. TiS: Methodology, Writing – review & editing. MR: Writing – review &

editing, Formal analysis, Methodology, Validation, Investigation, Resources.

Funding

The author(s) declared that financial support was received for this work and/or its publication. São Paulo Research Foundation (FAPESP) for the grants 2021/07007-7, 2022/06485-5, 2023/14250-0, 2023/17293-2, 2023/04501-6, 2022/11586-5, and 2023/10680-0. National Council for Scientific and Technological Development (CNPq) for the grants PIBIC 135207/2012-6, PIBIC 2022-3072, and 131500/2023-6. Coordination for the Improvement of Higher Education Personnel (CAPES), Brazil, 001.

Acknowledgments

We thank the São Paulo Research Foundation (FAPESP) for the grants 2021/07007-7, 2022/06485-5, 2023/14250-0, 2023/17293-2, 2023/04501-6, 2022/11586-5, and 2023/10680-0. We also acknowledge the National Council for Scientific and Technological Development (CNPq) for the grants PIBIC 135207/2012-6, PIBIC 2022-3072 and 131500/2023-6. SLB acknowledges the Coordination for the Improvement of Higher Education Personnel (CAPES), Brazil, 001. GLO thanks the support given by the Postdoctoral Programme and the Collaborating Researcher Programme from the University of São Paulo (Institute of Physics). We would like to thank Dr. Marilin Calo for help in the acquisition and processing of radiographies, Aline Bellenzani, Mônica Colacique, Vitória Souza, Dr. Cibele Voltani, Gabriel Leite, M.Sc. Juliana Bovolenta, M.Sc. Elizabeth Kajiya and Maria Alice Costa Negreiros for helping in photography, and M.Sc. Lorena Santos for assistance in image processing. We are grateful to Prof. Claudio Campi de Castro and to the University of São Paulo Hospital (HU-USP) technical staff for enabling radiography imaging. We thank the Laboratory of Materials Analyses by Ionic Beams (LAMFI-USP) and Marcos Antonio and Renan de Assis for technical support in ionoluminescence imaging. We are also grateful to Prof. Fabio Rodrigues and to M.Sc. Evandro Silva for assistance in RS analyses at the Astrolab (Institute of Chemistry-USP). We are grateful to Prof. Mírian Liza Pacheco and Dr. Gabriel Gonçalves Silva for insightful discussions regarding Raman data. We thank Prof. Juliana Leme and Ivone Gonzales for the access to the Paleontological Collection from the Institute of Geosciences (USP). We acknowledge the International Atomic Energy Agency (IAEA) and Dr. Friedrich Menges for having, respectively, developed and made the software WinQxas and Spectragryph available for users.

Conflict of interest

The author(s) declared that this work was conducted in the absence of any commercial or financial relationships that could be construed as a potential conflict of interest.

Generative AI statement

The author(s) declared that generative AI was not used in the creation of this manuscript.

Any alternative text (alt text) provided alongside figures in this article has been generated by Frontiers with the support of artificial intelligence and reasonable efforts have been made to ensure accuracy, including review by the authors wherever possible. If you identify any issues, please contact us.

Publisher's note

Supplementary material

The Supplementary Material for this article can be found online at: https://www.frontiersin.org/articles/10.3389/fevo.2025.1669055/full#supplementary-material

References

Amorim, K. B., Afonso, J. W. L., Leme, J. D. M., Diniz, C. Q. C., Rivera, L. C. M., Gómez-Gutiérrez, J. C., et al. (2020). Sedimentary facies, fossil distribution and depositional setting of the late Ediacaran Tamengo Formation (Brazil). *Sedimentology* 67, 3422–3450. doi: 10.1111/sed.12749

Antunes, G. C., Warren, L. V., Okubo, J., Freitas, B. T., Inglez, L., Caetano-Filho, S., et al. (2023). Assessing the correlation between Ediacaran-Cambrian units of SW Gondwana: The Tagatiya Guazú (Itapucumi Group, Paraguay) and Tamengo (Corumbá Group, Brazil) formations. *J. South Am. Earth Sci.* 130, 104577. doi: 10.1016/j.jsames.2023.104577

Arai, M., and Assine, M. L. (2020). Chronostratigraphic constraints and paleoenvironmental interpretation of the Romualdo Formation (Santana Group, Araripe Basin, Northeastern Brazil) based on palynology. *Cretaceous Res.* 116, 104610. doi: 10.1016/j.cretres.2020.104610

Assine, M. L., Neumann, H., Varejão, F. G., and Mescolotti, P. C. (2014). Sequências deposicionais do Andar Alagoas da Bacia do Araripe, Nordeste do Brasil, *B. Geoci.* Petrobras, 22(1), 3-28.

Barling, N., Martill, D. M., and Heads, S. W. (2020). A geochemical model for the preservation of insects in the Crato Formation (Lower Cretaceous) of Brazil. *Cretaceous Res.* 116, 104608. doi: 10.1016/j.cretres.2020.104608

Barling, N., Martill, D. M., Heads, S. W., and Gallien, F. (2015). High fidelity preservation of fossil insects from the Crato Formation (Lower Cretaceous) of Brazil. *Cretaceous Res.* 52, 605–622. doi: 10.1016/j.cretres.2014.05.007

Barling, N. T., Heads, S. W., and Martill, D. M. (2021). Behavioural impacts on the taphonomy of dragonflies and damselflies (Odonata) from the Lower Cretaceous Crato Formation, Brazil. *PE* 4, 141–155. doi: 10.11646/palaeoentomology.4.2.3

Bezerra, F. I., Da Silva, J. H., Agressot, E. V. H., Freire, P. T. C., Viana, B. C., and Mendes, M. (2023). Effects of chemical weathering on the exceptional preservation of mineralized insects from the Crato Formation, Cretaceous of Brazil: implications for late diagenesis of fine-grained Lagerstätten deposits. *Geol. Mag* 160, 911–926. doi: 10.1017/s0016756823000043

Bezerra, F. I., Da Silva, J. H., Miguel, E. D. C., Paschoal, A. R., Nascimento, D. R., Freire, P. T. C., et al. (2020). Chemical and mineral comparison of fossil insect cuticles from Crato Konservat Lagerstätte, Lower Cretaceous of Brazil. *J. Iber Geol* 46, 61–76. doi: 10.1007/s41513-020-00119-y

Bezerra, F. I., Silva, J. H. D., Paula, A. J. D., Oliveira, N. C., Paschoal, A. R., Freire, P. T. C., et al. (2018). Throwing light on an uncommon preservation of Blattodea from the Crato Formation (Araripe Basin, Cretaceous), Brazil. *Rev. Bras. Paleontologia* 21, 245–254. doi: 10.4072/rbp.2018.3.05

Bezerra, F. I., Solórzano-Kraemer, M. M., and Mendes, M. (2021). Distinct preservational pathways of insects from the Crato Formation, Lower Cretaceous of the Araripe Basin, Brazil. *Cretaceous Res.* 118, 104631. doi: 10.1016/j.cretres.2020.104631

Boderau, M., Jouault, C., Aracheloff, C., Ngô-Muller, V., Engel, M. S., Berthier, S., et al. (2024). Morphological and palaeoecological aspects of fossil insects unveiled by UV-A light. *MethodsX* 13, 102794. doi: 10.1016/j.mex.2024.102794

Boggs, S., and Krinsley, D. (2006). "Instrumentation and techniques," in *Application of Cathodoluminescence Imaging to the Study of Sedimentary Rocks*. Eds. S. Boggs and D. Krinsley (Cambridge University Press, New York), 19–46.

Bowyer, F., Wood, R. A., and Poulton, S. W. (2017). Controls on the evolution of Ediacaran metazoan ecosystems: A redox perspective. *Geobiology* 15, 516–551. doi: 10.1111/gbi.12232

Bryant, R. N., Pasteris, J. D., and Fike, D. A. (2018). Variability in the raman spectrum of unpolished growth and fracture surfaces of pyrite due to laser heating and crystal orientation. *Appl. Spectrosc* 72, 37–47. doi: 10.1177/0003702817736516

Buscalioni, Á.D., Umamaheswaran, R., Sánchez-García, A., López-Archilla, A. I., Dias, J. J., De Souza Carvalho, I., et al. (2025). Exceptional preservation in mayfly nymphs (Insecta: Ephemeroptera) from the Early Cretaceous of the Las Hoyas fossil site. *Cretaceous Res.* 167, 106052. doi: 10.1016/j.cretres.2024.106052

Bushberg, J. T., Seibert, J. A., Leidholdt, E. M., and Boone, J. M. (2011). "*The Essential Physics of Medical Imaging*,", *3rd Edn* (Lippincott Williams & Wilkins, Philadelphia). Available online at: https://books.google.com/books/about/The_Essential_Physics_of_Medical_Imagin.html?id=wFtFAQAAQBAJ.

Calderon, T. (2008). Ionoluminescence and minerals: the state of the art. *Rev. Mexicana Física* 54, 21–28.

Carrier, B. L., Abbey, W. J., Beegle, L. W., Bhartia, R., and Liu, Y. (2019). Attenuation of ultraviolet radiation in rocks and minerals: implications for mars science. *JGR Planets* 124, 2599–2612. doi: 10.1029/2018je005758

Carvalho, I. S., Dias, J. J., Silva, D. S., Borghi, L., Andrade, J. A. F. G., Viana, M. S. S., et al. (2024a). "A new dinosaur tracksite from the Araripe Basin (Brazil) and the putative Early Paleozoic age for the Mauriti Formation," in *New Mexico Museum of Natural History and Science Bulletin*, 339–344. doi: 10.1007/978-3-031-56355-3_6

Carvalho, I. S., Leonardi, G., and Dias, J. J. (2024b). "The Cretaceous Araripe Basin dinosaur tracks and their paleoenvironmental meaning," in *Dinosaur Tracks of Mesozoic Basins in Brazil: Impact of Paleoenvironmental and Paleoclimatic Changes*. Eds. I. S. Carvalho and G. Leonardi (Springer, Cham), 147–178. doi: 10.1007/978-3-031-56355-3_6

Carvalho, M. G. P., Maisey, J. G., Mendes, I. D., and De Souza Carvalho, I. (2023). Micro-tomographic analysis of a scorpion fossil from the Aptian Crato Formation of Northeastern Brazil. *Cretaceous Res.* 147, 105454. doi: 10.1016/j.cretres.2022.105454

Castillo, H. C., Del Millán, A., Beneítez, P., Ruvalcaba–Sil, J. L., and Calderón, T. (2008). Proton induced luminescence of minerals. *Rev. Mexicana Física* 54, 93–99.

Chen, J., Li, H., Yuan, Y., Zhang, M., Shuai, S., and Wan, J. (2022). Raman spectroscopic studies of pyrite at high pressure and high temperature. *Minerals* 12, 332. doi: 10.3390/min12030332

Choi, S., Lee, S. K., Kim, N.-H., Kim, S., and Lee, Y.-N. (2020). Raman spectroscopy detects amorphous carbon in an enigmatic egg from the upper cretaceous wido volcanics of South Korea. *Front. Earth Sci.* 7. doi: 10.3389/feart.2019.00349

Courtois, J.-Y. (1993). Spectroscopie Raman et Rayleigh stimulée d'atomes refroidis par laser: dynamique des mélasses optiques unidimensionnelles. *Physique Atomique*. Ecole Polytechnique X.

Crippa, G., and Masini, S. (2022). Photography in the ultraviolet and visible violet spectra: unravelling methods and applications in palaeontology. *APP* 67, 685–702. doi: 10.4202/app.00948.2021

Crowther, J. (2022). Ultraviolet fluorescence photography—Choosing the correct filters for imaging. *J. Imaging* 8, 162. doi: 10.3390/jimaging8060162

Curry, T. S., Dowdey, J. E., Murry, R. C., and Christensen, E. E. (1990). *Christensen's physics of diagnostic radiology*. *4th ed* (Philadelphia: Lea & Febiger).

De Faria, D. L. A., Venâncio Silva, S., and De Oliveira, M. T. (1997).). Raman microspectroscopy of some iron oxides and oxyhydroxides. *J. Raman Spectrosc* 28, 873–878. doi: 10.1002/(sici)1097-4555(199711)28:11<873::aid-jrs177>3.0.co;2-b

Delgado, A. D. O., Buck, P. V., Osés, G. L., Ghilardi, R. P., Rangel, E. C., and Pacheco, M. L. A. F. (2014). Paleometry: A brand new area in Brazilian science. *Mat. Res.* 17, 1434–1441. doi: 10.1590/1516-1439.288514

Delsett, L. L., Friis, H., Kölbl-Ebert, M., and Hurum, J. H. (2022). The soft tissue and skeletal anatomy of two Late Jurassic ichthyosaur specimens from the Solnhofen archipelago. *PeerJ* 10, e13173. doi: 10.7717/peerj.13173

Dias, J., Batista, D., Corecco, L., and Carvalho, I. (2022). "Bacia do Araripe: Biotas do Cretáceo do Gondwana," *Paleontologia do Brasil: Paleoecologia e Paleoambientes* (Editora Interciência, Rio de Janeiro), 129–190.

Dias, J. J., and Carvalho, I. D. S. (2020). Remarkable fossil crickets preservation from Crato Formation (Aptian, Araripe Basin), a Lagerstätten from Brazil. *J. South Am. Earth Sci.* 98, 102443. doi: 10.1016/j.jsames.2019.102443

Dias, J. J., and Carvalho, I. D. S. (2022). The role of microbial mats in the exquisite preservation of Aptian insect fossils from the Crato Lagerstätte, Brazil. *Cretaceous Res.* 130, 105068. doi: 10.1016/j.cretres.2021.105068

Dias, J. J., Carvalho, I. D. S., Souza-Dias, P. G. B., Zefa, E., Barros, C. D. L., Prado, G., et al. (2025). Reproductive organs of a Grylloidea fossil from the Cretaceous Araripe Basin, Brazil. *JGS* 182. doi: 10.1144/jgs2024-211

Dias, J. J., De Souza Carvalho, I., Buscalioni, Á.D., Umamaheswaran, R., López-Archilla, A. I., Prado, G., et al. (2023). Mayfly larvae preservation from the Early Cretaceous of Brazilian Gondwana: Analogies with modern mats and other Lagerstätten. *Gondwana Res.* 124, 188–205. doi: 10.1016/j.gr.2023.07.007

Diniz, C. Q. C., Leme, J. D. M., and Boggiani, P. C. (2021). New species of macroalgae from tamengo formation, ediacaran, Brazil. *Front. Earth Sci.* 9. doi: 10.3389/feart.2021.748876

El Ali, A., Barbin, V., Calas, G., Cervelle, B., Ramseyer, K., and Bouroulec, J. (1993). Mn2+-activated luminescence in dolomite, calcite and magnesite: quantitative determination of manganese and site distribution by EPR and CL spectroscopy. *Chem. Geology* 104, 189–202. doi: 10.1016/0009-2541(93)90150-h

Endrizzi, M. (2018). X-ray phase-contrast imaging. *Nucl. Instrum. Methods Phys. Res. A* 878, 88. doi: 10.1016/j.nima.2017.07.036

England, J., Cusack, M., Paterson, N. W., Edwards, P., Lee, M. R., and Martin, R. (2006). Hyperspectral cathodoluminescence imaging of modern and fossil carbonate shells. *J. Geophys. Res.* 111. doi: 10.1029/2005jg000144

Enguita, O., Calderón, T., Fernández-Jiménez, M. T., Beneitez, P., Millan, A., and Garcıa, G. (2004). Damage induced by proton irradiation in carbonate based natural painting pigments. *Nucl. Instruments Methods Phys. Res. Section B: Beam Interact. Materials Atoms* 219–220, 53–56. doi: 10.1016/j.nimb.2004.01.027

Feng, X., Xie, Y., Zhao, W., Green, M., Liu, L., and Chen, X. (2021). Fluorescence quenching effects of Fe3+ ions on carbon dots. *Spectroscopy* 36, 31–36.

Frese, M., Gloy, G., Oberprieler, R. G., and Gore, D. B. (2017). Imaging of Jurassic fossils from the Talbragar Fish Bed using fluorescence, photoluminescence, and elemental and mineralogical mapping. *PloS One* 12, e0179029. doi: 10.1371/journal.pone.0179029

Frost, R. L., Wills, R.-A., Weier, M. L., Martens, W., and Mills, S. (2006). A Raman spectroscopic study of selected natural jarosites. *Spectrochimica Acta Part A: Mol. Biomolecular Spectrosc.* 63, 1–8. doi: 10.1016/j.saa.2005.03.034

Gaft, M., Reisfeld, R., and Panczer, G. (2015). Modern luminescence spectroscopy of minerals and materials. (Springer), 625 p. doi: 10.1007/978-3-319-24765-6

Grimaldi, D. A. (2005). *Evolution of the insects* (Cambridge, UK: Cambridge University Press).

Hahn, G., Hahn, R., Leonardos, H. D., Pflug, H. D., and Walde, H. G. (1982). Körperlich erhaltene Scyphozoen-Reste aus dem Jungpräkambrium Brasiliens. *Geologica palaeontologica* 16, 1–18.

Haug, C., Haug, J. T., Waloszek, D., Maas, A., Frattigiani, R., and Liebau, S. (2009). New methods to document fossils from lithographic limestones of southern Germany and Lebanon. *Palaeontologia Electronica* 12, 6–12.

Heads, S. W., and Martins-Neto, R. G. (2007). "Orthopterida: grasshoppers, crickets, locusts and stick insects," in *The Crato Fossil Beds of Brazil: Window to an Ancient World*. Eds. D. M. Martill, G. Bechly and R. Loveridge (Cambridge University Press, New York), 265–282.

Hone, D. W. E., Tischlinger, H., Xu, X., and Zhang, F. (2010). The Extent of the Preserved Feathers on the Four-Winged Dinosaur Microraptor gui under Ultraviolet Light. *PloS One* 5, e9223. doi: 10.1371/journal.pone.0009223

Huda, W., and Abrahams, R. B. (2015). Radiographic techniques, contrast, and noise in X-ray imaging. *Am. J. Roentgenology* 204, W126–W131. doi: 10.2214/ajr.14.13116

Iniesto, M., Gutiérrez-Silva, P., Dias, J. J., Carvalho, I. S., Buscalioni, A. D., and López-Archilla, A. I. (2021). Soft tissue histology of insect larvae decayed in laboratory experiments using microbial mats: Taphonomic comparison with Cretaceous fossil insects from the exceptionally preserved biota of Araripe, Brazil. *Palaeogeography Palaeoclimatology Palaeoecol.* 564, 110156. doi: 10.1016/j.palaeo.2020.110156

IUPAC (2025). *Compendium of Chemical Terminology: Luminescence*. *5th Edn* (International Union of Pure and Applied Chemistry). doi: 10.1351/goldbook.L03641

Jenkins, R. (1999). "Analytical X-ray for Industry and Science," in *The 11th National School and Conference of the Australian X-ray Analytical Association on Analytical X-ray for Industry and Science*, vol. 12. (Australian X-ray Analytical Association, Melbourne, Austrália). Available online at: https://www.osti.gov/biblio/6070139.

Kelley, P. H., and Swann, C. T. (1988). Functional significance of preserved color patterns of mollusks from the Gosport Sand (Eocene) of Alabama. *J. Paleontol* 62, 83–87. doi: 10.1017/s0022336000018035

Klug, C., Di Silvestro, G., Hoffmann, R., Schweigert, G., Fuchs, D., Clements, T., et al. (2021a). Taphonomic patterns mimic biologic structures: diagenetic Liesegang rings in Mesozoic coleoids and coprolites. *PeerJ* 9, e10703. doi: 10.7717/peerj.10703

Klug, C., Landman, N. H., Fuchs, D., Mapes, R. H., Pohle, A., Guériau, P., et al. (2019). Anatomy and evolution of the first Coleoidea in the Carboniferous. *Commun. Biol.* 2. doi: 10.1038/s42003-019-0523-2

Klug, C., Schweigert, G., Fuchs, D., Kruta, I., and Tischlinger, H. (2016). Adaptations to squid-style high-speed swimming in Jurassic belemnitids. *Biol. Lett.* 12, 20150877. doi: 10.1098/rsbl.2015.0877

Klug, C., Schweigert, G., Tischlinger, H., and Pochmann, H. (2021b). Failed prey or peculiar necrolysis? Isolated ammonite soft body from the Late Jurassic of Eichstätt (Germany) with complete digestive tract and male reproductive organs. *Swiss J. Palaeontol* 140. doi: 10.1186/s13358-020-00215-7

Kusano, N., Nishido, H., and Inoue, K. (2014). Cathodoluminescence of calcite decomposed from dolomite in high–temperature skarn. *J. Mineralogical Petrological Sci.* 109, 286–290. doi: 10.2465/jmps.140612

Lang, J., and Middleton, A. (2005). *Radiography of Cultural Immaterial. 2nd Edn* (New York: Routledge).

Langland, O. E., Langlais, R. P., and Preece, J. W. (2002). *Principles of Dental Imaging. 2nd Edn* (Baltimore: Lippincott Williams & Wilkins).

Lewis, I. R., and Edwards, H. (2001). Handbook of Raman Spectroscopy: From the Research Laboratory to the Process Line (Boca Raton, FL,CRC Press). Available online at: https://books.google.com.br/books?id=E9peWTnT9TgC (Accessed July 17, 2025).

Liu, D., Chiappe, L. M., Zhang, Y., Serrano, F. J., and Meng, Q. (2019). Soft tissue preservation in two new enantiornithine specimens (Aves) from the Lower Cretaceous Huajiying Formation of Hebei Province, China. *Cretaceous Res.* 95, 191–207. doi: 10.1016/j.cretres.2018.10.017

Liu, C., Ling, Z., Zhang, J., Bi, X., and Cao, F. (2020). Laboratory Raman and VNIR spectroscopic studies of jarosite and other secondary mineral mixtures relevant to Mars. *J. Raman Spectrosc* 51, 1575–1588. doi: 10.1002/jrs.5809

Machel, H. G. (2000). "Application of Cathodoluminescence to Carbonate Diagenesis," in *Cathodoluminescence in geosciences*, vol. 271–301 . Ed. M. Pagel (Springer, Berlin, Heidelberg, [Germany]).

Maldanis, L., Carvalho, M., Almeida, M. R., Freitas, F. I., De Andrade, J. A. F. G., Nunes, R. S., et al. (2016). Heart fossilization is possible and informs the evolution of cardiac outflow tract in vertebrates. *eLife* 5. doi: 10.7554/elife.14698

McCollough, C. H. (1997). The AAPM/RSNA physics tutorial for residents. X-ray production. *RadioGraphics* 17, 967–984. doi: 10.1148/radiographics.17.4.9225393

Menges, F. (2022). *Spectragryph - optical spectroscopy software, Version 1.2.16.1.*

Moura-Júnior, D. A., Scheffler, S. M., and Fernandes, A. C. S. (2018). The Brazilian fossil insects: current scenario. *Anuário IGEO UFRJ* 41, 142–166. doi: 10.11137/2018_1_142_166

Nair, G. B., and Dhoble, S. J. (2020). *The Fundamentals and Applications of Light-Emitting Diodes: The Revolution in the Lighting Industry*. Duxford, UK: Elsevier. doi: 10.1016/C2019-0-00273-7

Oliveira, R. S. D., Nogueira, A. C. R., Romero, G. R., Truckenbrodt, W., and Da Silva Bandeira, J. C. (2019). Ediacaran ramp depositional model of the Tamengo Formation, Brazil. *J. South Am. Earth Sci.* 96, 102348. doi: 10.1016/j.jsames.2019.102348

Osés, G. L., Afonso, J. W. L., Wood, R. A., Freitas, B. T., Romero, G. R., Paula-Santos, G. M., et al. (2025). Clastic sedimentary record impacted by carbonate bioclasts in the Late Ediacaran. *Geol. Mag* 162. doi: 10.1017/s0016756824000335

Osés, G. L., Petri, S., Becker-Kerber, B., Romero, G. R., Rizzutto, M. D. A., Rodrigues, F., et al. (2016). Deciphering the preservation of fossil insects: a case study from the Crato Member, Early Cretaceous of Brazil. *PeerJ* 4, e2756. doi: 10.7717/peerj.2756

Osés, G. L., Petri, S., Voltani, C. G., Prado, G. M. E. M., Galante, D., Rizzutto, M. A., et al. (2017). Deciphering pyritization-kerogenization gradient for fish soft-tissue preservation. *Sci. Rep.* 7. doi: 10.1038/s41598-017-01563-0

Osés, G. L., Wood, R., Romero, G. R., Evangelista Martins Prado, G. M., Bidola, P., Herzen, J., et al. (2022). Ediacaran *Corumbella* has a cataphract calcareous skeleton with controlled biomineralization. *iScience* 25, 105676. doi: 10.1016/j.isci.2022.105676

Pacheco, M. L. A. F., Galante, D., Rodrigues, F., Leme, J., Bidola, P., Hagadorn, W., et al. (2015). Insights into the Skeletonization, Lifestyle, and Affinity of the Unusual Ediacaran Fossil Corumbella. *PLOS ONE* 10 (3), e0114219. doi: 10.1371/journal.pone.0114219

Paes-Neto, V. D., Parkinson, A. H., Pretto, F. A., Soares, M. B., Schwanke, C., Schultz, C. L., et al. (2016). Oldest evidence of osteophagic behavior by insects from the Triassic of Brazil. *Palaeogeography Palaeoclimatology Palaeoecol.* 453, 30–41. doi: 10.1016/j.palaeo.2016.03.026

Parry, L. A., Boggiani, P. C., Condon, D. J., Garwood, R. J., Leme, J. D. M., McIlroy, D., et al. (2017). Ichnological evidence for meiofaunal bilaterians from the terminal Ediacaran and earliest Cambrian of Brazil. *Nat. Ecol. Evol.* 1, 1455–1464. doi: 10.1038/s41559-017-0301-9

Pedone, V. A., Cercone, K. R., and Burruss, R. C. (1990). Activators of photoluminescence in calcite: evidence from high-resolution, laser-excited luminescence spectroscopy. *Chem. Geology* 88, 183–190. doi: 10.1016/0009-2541(90)90112-k

Prado, G., Arthuzzi, J. C. L., Osés, G. L., Callefo, F., Maldanis, L., Sucerquia, P., et al. (2021). Synchrotron radiation in palaeontological investigations: Examples from Brazilian fossils and its potential to South American palaeontology. *J. South Am. Earth Sci.* 108, 102973. doi: 10.1016/j.jsames.2020.102973

Prasad, P. S. R., Pradhan, A., and Gowd, T. N. (2001). *In situ* micro-Raman investigation of dehydration mechanism in natural gypsum. *Curr. Sci.* 80, 1203–1207.

Ribeiro, A. C., Ribeiro, G. C., Varejão, F. G., Battirola, L. D., Pessoa, E. M., Simões, M. G., et al. (2021). Towards an actualistic view of the Crato Konservat-Lagerstätte paleoenvironment: A new hypothesis as an Early Cretaceous (Aptian) equatorial and semi-arid wetland. *Earth-Science Rev.* 216, 103573. doi: 10.1016/j.earscirev.2021.103573

Riquelme, F., Ruvalcaba Sil, J. L., and Alvarado Ortega, J. (2009). Palaeometry: Non-destructive analysis of fossil materials. *BSGM* 61, 177–183. doi: 10.18268/bsgm2009v61n2a4

Romppanen, S., Häkkänen, H., and Kaski, S. (2021). Laser-induced time-resolved luminescence in analysis of rare earth elements in apatite and calcite. *J. Luminescence* 233, 117929. doi: 10.1016/j.jlumin.2021.117929

Sasaki, K., Tanaike, O., and Konno, H. (1998). Distinction of jarosite-group compaunds by Raman spectroscopy. *Can. Mineralogist* 36, 1225–1235.

Sasan, S., Chopra, T., Gupta, A., Tsering, D., Kapoor, K. K., and Parkesh, R. (2022). Fluorescence "Turn-off" and colorimetric sensor for fe^{2+}, fe^{3+}, and cu^{2+} Ions based on a 2,5,7-triarylimidazopyridine scaffold. *ACS Omega*. 7 (13), 11114-11125. doi: 10.1021/acsomega.1c07193

Schueler, B. A. (1998). Clinical applications of basic x-ray physics principles. *RadioGraphics* 18, 731–744. doi: 10.1148/radiographics.18.3.9599394

Schwermann, A. H., Dos Santos Rolo, T., Caterino, M. S., Bechly, G., Schmied, H., Baumbach, T., et al. (2016). Preservation of three-dimensional anatomy in phosphatized fossil arthropods enriches evolutionary inference. *eLife* 5. doi: 10.7554/elife.12129

Selden, P., and Nudds, J. (2012). *Evolution of Fossil Ecosystems. 2nd Edn* (Amsterdam: CRC Press). doi: 10.1016/C2012-0-01282-3

Silva, T. F., Rodrigues, C. L., Added, N., Rizzutto, M. A., Tabacniks, M. H., Mangiarotti, A., et al. (2018). Elemental mapping of large samples by external ion beam analysis with sub-millimeter resolution and its applications. *Nucl. Instrum. Methods Phys. Res. B* 422, 68–77. doi: 10.1016/j.nimb.2018.03.006

Sites, R. W. (2022). Phylogeny and revised classification of the saucer bugs (Hemiptera: Nepomorpha: Naucoridae). *Zoological J. Linn. Soc.* 195, 1245–1286. doi: 10.1093/zoolinnean/zlab105

Šoster, A., Bertrandsson Erlandsson, V., Velojić, M., and Gopon, P. (2023). Ultraviolet-photoluminescence and trace element analyses in Ga-rich sphalerite from the Djebel Gustar Zn–Pb deposit, Algeria. *Ore Geol. Rev.* 157, 105474. doi: 10.1016/j.oregeorev.2023.105474

Stoneman, M. R., McCoy, V. E., Gee, C. T., Bober, K. M. M., and Raicu, V. (2024). Two-photon excitation fluorescence microspectroscopy protocols for examining fluorophores in fossil plants. *Commun. Biol.* 7. doi: 10.1038/s42003-024-05763-z

Storari, A. P., Osés, G. L., Almeida-Lima, D. S. D., Rizzutto, M. A., Bantim, R. A. M., Lima, F. J. D., et al. (2024a). Exceptionally well-preserved orthopteran proventriculi from the Cretaceous Crato Formation of Brazil. *J. South Am. Earth Sci.* 133, 104737. doi: 10.1016/j.jsames.2023.104737

Storari, A. P., Osés, G. L., Staniczek, A. H., Rizzutto, M., Loeffler, R., and Rodrigues, T. (2024b). Paleometric approaches reveal striking differences in the insect fossilization of two Mesozoic Konservat-Lagerstätten. *Front. Ecol. Evol.* 12. doi: 10.3389/fevo.2024.1445160

Storari, A. P., Rodrigues, T., Bantim, R. A. M., Lima, F. J., and Saraiva, A. A. F. (2021). Mass mortality events of autochthonous faunas in a Lower Cretaceous Gondwanan Lagerstätte. *Sci. Rep.* 11. doi: 10.1038/s41598-021-85953-5

Sy, E., Samboju, V., and Mukhdomi, T. (2022). "X-ray Image Production Procedures," in *StatPearls* (StatPearls Publishing, Treasure Island (FL). Available online at: https://www.ncbi.nlm.nih.gov/books/NBK564352/.

Tischlinger, H., and Arratia, G. (2013). "Ultraviolet light as a tool for investigating Mesozoic fishes, with a focus on the ichthyofauna of the Solnhofen archipelago," in *Mesozoic Fishes – Global Diversity and Evolution* (F. Pfeil, München), 549–560.

Tompe, A., and Sargar, K. (2022). "X-Ray Image Quality Assurance," in *StatPearls* (StatPearls Publishing, Treasure Island (FL). Available online at: https://www.ncbi.nlm.nih.gov/books/NBK580506/.

Tonnessen, B. H., and Pounds, L. (2011). Radiation physics. *J. Vasc. Surg.* 53, 6S–8S. doi: 10.1016/j.jvs.2010.05.138

Vallejo, J. D., Piovesan, E. K., De Araujo Carvalho, M., and Guzmán, J. (2023). Palynofacies analyses of Santana Group, upper Aptian of the Araripe Basin, northeast Brazil: Paleoenvironmental reconstruction. *J. South Am. Earth Sci.* 121, 104154. doi: 10.1016/j.jsames.2022.104154

Vandenabeele, P. (2013). Practical Raman Spectroscopy: An Introduction (Chichester, West Sussex, UK: John Wiley & Sons). Available online at: https://books.google.com.br/books?id=HjFi5eOUYvgC (Accessed July 17, 2025).

Van Grieken, R. E., and Markowicz, A. A. (2001). *Handbook of X-ray Spectrometry. 2. ed* (New York, N.Y: CRC Press).

Van Iten, H., Leme, J., Pacheco, M. L. A. F., and Simoes, M. G. (2016). "Origin and Early Diversification of Phylum Cnidaria: Key Macrofossils from the Ediacaran System of North and South America," in *The Cnidaria, Past, Present and Future* (Springer, Cham), 31–40. doi: 10.1007/978-3-319-31305-4_3

Varejão, F. G., Warren, L. V., Simões, M. G., Fürsich, F. T., Matos, S. A., and Assine, M. L. (2019). Exceptional preservation of soft tissues by microbial entombment: Insights into the taphonomy of the Crato Konservat-Lagerstätte. *PALAIOS* 34, 331–348. doi: 10.2110/palo.2019.041

Wang, X., Pittman, M., Zheng, X., Kaye, T. G., Falk, A. R., Hartman, S. A., et al. (2017). Basal paravian functional anatomy illuminated by high-detail body outline. *Nat. Commun.* 8. doi: 10.1038/ncomms14576

White, S. C., and Pharoah, M. J. (2013). *Oral Radiology: Principles and Interpretation. 7th ed* (St. Louis: Mosby).

Williams, M. B., Krupinski, E. A., Strauss, K. J., Breeden, W. K., Rzeszotarski, M. S., Applegate, K., et al. (2007). Digital radiography image quality: image acquisition. *J. Am. Coll. Radiol.* 4, 371–388. doi: 10.1016/j.jacr.2007.02.002

Wolkenstein, K. (2022). Fluorescent colour patterns in the basal pectinid Pleuronectites from the Middle Triassic of Central Europe: origin, fate and taxonomic implications of fluorescence. *Palaeontology* 65. doi: 10.1111/pala.12625

Wolkenstein, K., Schmidt, B. C., and Harzhauser, M. (2024). Detection of intact polyene pigments in Miocene gastropod shells. *Palaeontology* 67. doi: 10.1111/pala.12691

Wood, R. (2018). Exploring the drivers of early biomineralization. *Emerging Topics Life Sci.* 2, 201–212. doi: 10.1042/etls20170164

Yang, C., Homman, N. P.-O., Malmqvist, K. G., Johansson, L., Halden, N. M., and Barbin, V. (1994). Ionoluminescence: A new tool for nuclear microprobes in geology. *Scanning Microscopy* 9, 1.

Zaine, M. F., and Fairchild, T. R. (1985). Comparison of Aulophycus lucianoi beurlen and sommer from Ladário (MS) and the genus *Cloudina* germs, Edicaran of Namibia. *Anais da Academia Bras. Ciências* 57, 130.

Zangerl, R. (1965). "Radiographic techniques," in *Handbook of Paleontological Techniques*. Eds. B. Kummel and D. Raup (W.H. Freeman and Company, San Francisco), 305–320.